# Technical Note: DACNO$_2$ – A Multi-Constraint Deep Learning Framework for High-Resolution 3D NO$_2$ Field Estimation

Wenfu Sun[1, 2], Frederik Tack[1], Lieven Clarisse[2], Michel Van Roozendael[1]

[1] Royal Belgian Institute for Space Aeronomy (BIRA-IASB), Brussels, Belgium.
[2] Université libre de Bruxelles (ULB), Spectroscopy, Quantum Chemistry and Atmospheric Remote Sensing (SQUARES), Brussels, Belgium.

Correspondence to: Wenfu Sun (wenfu.sun@aeronomie.be)

**Abstract.** ~~Accurate, high~~High-resolution 3D fields of nitrogen dioxide ($NO_2$) are critical for air quality management and satellite retrievals, yet traditional chemistry-transport models (CTMs) face challenges in fine-scale modeling. Machine learning (ML) alternatives often struggle with generalization and transferability, inheriting biases from CTMs or being limited by sparse surface measurements. We present the Deep Atmospheric Chemistry $NO_2$ model (DACNO$_2$), a deep learning model that generates daily 2 km × 2 km 3D $NO_2$ fields over Western Europe. The model's three-phase ~~and~~ multi-constraint training strategy begins by pre-training on European Copernicus Atmosphere Monitoring Service (CAMS) reanalysis data to learn large-scale atmospheric patterns, then fine-tunes with ~~both~~ CAMS and in-situ European Environmental Agency (EEA) surface data to correct biases and refine local detail, and completes with an adaptive fine-tuning to capture evolving trends. An evaluation for 2023 shows that DACNO$_2$ reproduces broad-scale 3D CAMS fields ($R^2 = 0.90$) ~~while improving~~and improves agreement with independent EEA stations over the CAMS reanalysis ($R^2$ enhanced from 0.61 to 0.66; bias reduced from -1.15 to -0.38 µg/m$^3$). The model resolves ~~more~~ spatial ~~detail~~details and ~~learns~~exhibits physically ~~interpretable relationships~~plausible behavior. This hybrid training approach fuses the physical consistency of a process-based model with the real-world ~~accuracy of~~ surface measurements, overcoming the limitations of using either constraint ~~data~~ alone. Applying DACNO$_2$ a-priori profiles to TROPOMI retrievals increases tropospheric $NO_2$ columns by 3% on average over those using European CAMS profiles, with ~~larger enhancements over emission hotspots.~~enhanced contrast between low- and high-$NO_2$ regions, primarily attributable to improved resolution. These results demonstrate the framework's potential to advance air quality monitoring and satellite remote sensing.

## 1. Introduction

Nitrogen dioxide ($NO_2$) is a key atmospheric pollutant with significant impacts on air quality, human health, ecosystems, and atmospheric chemistry. Primary sources include traffic, industrial activities, and energy production, with additional contributions from natural emissions (Crippa et al., 2018). Accurate characterization of the spatiotemporal distribution of $NO_2$ is critical for both air pollution management and atmospheric chemistry research.

Chemistry Transport Models (CTMs) such as GEOS-Chem (Bey et al., 2001), TM5-MP (Krol et al., 2005; Williams et al., 2017; Huijnen et al., 2010), WRF-Chem (Grell et al., 2005), and the Copernicus Atmosphere Monitoring Service (CAMS) (Peuch et al., 2022; Inness et al., 2019) are widely used to simulate atmospheric $NO_2$ based on physical and chemical processes. However, most CTMs operate at coarse spatial resolution due to computational constraints and the limited availability of high-resolution emission inventories. This restricts their ability to represent fine-scale $NO_2$ variability and often results in spatial smoothing and underestimation, particularly in urban environments. Emission inventories are usually outdated and may omit localized and small-scale sources ~~(Lu et al., 2025)~~(Lu et al., 2025), contributing to uncertainties and discrepancies between bottom-up and top-down emission estimates (Kuik et al., 2018; Yang et al., 2021). While regional high-resolution CTMs are available, such as CAMS at 10 km × 10 km resolution (Douros et al., 2023; Ialongo et al., 2020) and regional WRF-Chem at 3 km ~~(Kuhn et al., 2024b)~~× 3 km resolution (Kuhn et al., 2024b), challenges remain in accurately capturing urban and fine-scale $NO_2$ patterns (Meleux et al., 2024), and model optimization is often resource-intensive (Kuhn et al., 2024a; Kuhn et al., 2024b).

CTM outputs also serve as a-priori $NO_2$ profiles for satellite retrievals (Palmer et al., 2001; Douros et al., 2023; Yang et al., 2023), supporting large-scale $NO_2$ monitoring. Over the past three decades, satellite $NO_2$ observations have been advancing toward higher spatiotemporal resolution. Satellite instruments such as the TROPOspheric Monitoring Instrument (TROPOMI, 7 km × 3.5 ~~km~~$^2$km, 5.5 km × 3.5 ~~km~~$^2$km since August 2019) on Sentinel-5P (Veefkind et al., 2012), the Geostationary Environment Monitoring Spectrometer (GEMS, 3.5 km × 8 ~~km~~$^2$km) (Kim et al., 2020), Tropospheric emissions: Monitoring of pollution (TEMPO, 2 km × 4.75 ~~km~~$^2$km) (Zoogman et al., 2017), Sentinel-4 (8 km × 8 ~~km~~$^2$km) (Gulde et al., 2017), Sentinel-5 (7.5 km × 7.5 ~~km~~$^2$km) (Bézy et al., 2014), Twin ANthropogenic Greenhouse Gas Observers (TANGO, 300 m × 300 ~~m~~$^2$m) (Landgraf et al., 2020), and the Copernicus Anthropogenic Carbon Dioxide Monitoring constellation (CO2M, 2 km × 2 ~~km~~$^2$km) (Bernd et al., 2021) are advancing spaceborne $NO_2$ observations to kilometer-scale resolution. This progress has increased

demand for high-resolution a- priori profiles, which can ~~improve the sensitivity of satellite $NO_2$ products to~~ better account for near-surface ~~concentrations~~$NO_2$ enhancements and strong spatial gradients over emission hotspots~~.~~ in satellite $NO_2$ retrieval products. It motivates us to develop a 3D $NO_2$ product on a 2 km × 2 km horizontal grid (hereafter referred to as the 2 km grid) to better resolve fine-scale spatial heterogeneity and support the emerging high-resolution satellite missions (e.g., CO2M). However, CTM-based profiles remain constrained by the limitations mentioned above, highlighting the need for alternative modeling approaches.

Machine learning (ML) provides an efficient alternative for high-resolution $NO_2$ estimation. ML techniques have been widely applied for surface $NO_2$ mapping (Sun et al., 2024; Kim et al., 2021; Wei et al., 2022), and recent studies have extended these approaches for 3D $NO_2$ modeling above the surface. These studies have trained models on process-based 3D $NO_2$ fields generated by CTMs (Bodnar et al., 2024; Kuhn et al., 2024a), on vertical profiles from MAX-DOAS observations (Zhang et al., 2025; Zhang et al., 2022b; Jiang et al., 2025), and on a combination of process-based ~~CTM outputs~~3D $NO_2$ fields with satellite observations (Li and Xing, 2024). While these studies demonstrate the feasibility of ML-based 3D $NO_2$ modeling, challenges remain in achieving high spatial resolution, robust generalization, and transferability. Process-based data carries inherent biases and has relatively coarse resolution. Ground-based observations are sparse and unevenly distributed, limiting the model's spatial generalization. While Li and Xing (2024) combine process-based $NO_2$ fields with satellite $NO_2$ observations from the Ozone Monitoring Instrument (OMI) to train the ML model, the resulting product is still limited to a coarse resolution (27 km × 27 km).

In this study, we present the Deep Atmospheric Chemistry $NO_2$ model ($DACNO_2$), a deep learning model developed to produce daily, high-resolution ~~(2 km)~~ 3D $NO_2$ fields on the 2 km grid with high accuracy, robust generalization, and transferability. $DACNO_2$ integrates multi-source inputs, including emissions, geography, meteorology, and temporal indicators. The model is trained using a phased, multi-constraint approach that combines process-based CAMS fields with ground-based EEA measurements. This method enables the model to reproduce broad-scale, process-based $NO_2$ patterns and capture local $NO_2$ gradients. The training strategy consists of three phases: pre-training, multi-constraint fine-tuning, and adaptive fine-tuning. Western Europe (5°W–9°E, 42°N–54°N) is chosen as the study region, given its diverse topography, high urbanization, and substantial industrial activity.

This study addresses two key research questions: (1) Can a deep learning framework combining multi-constraint and phased training overcome the resolution, bias, and generalization limitations of current CTM and ML approaches for 3D $NO_2$ modeling? (2) Does the DACNO$_2$ ~~2 km~~ product on the 2 km grid improve fine-scale $NO_2$ representation to support applications in regional air quality management and satellite retrievals?

The remainder of this paper is organized as follows. Section 2 describes the DACNO$_2$ development framework, including dataset preparation, model architecture, and training strategy. Section 3 evaluates model performance. Section 4 discusses broader insights and implications. Conclusions and outlook are provided in Section 5.

## 2. Development Framework for DACNO$_2$

### 2.1 Framework Overview

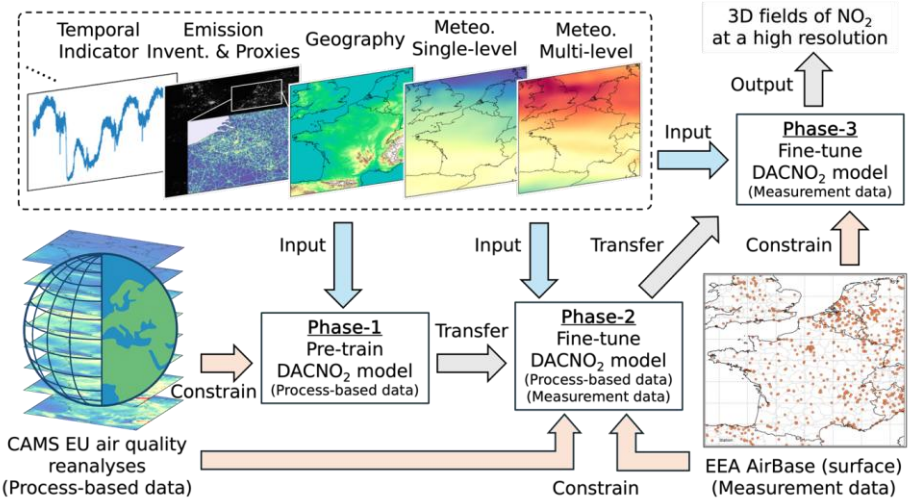


**Figure 1. Overview of the DACNO$_2$ model development framework. The framework integrates multiple input data streams: temporal indicators, emission inventories and proxies, geography, and ERA5 meteorological data, with two target datasets: process-based NO$_2$ from CAMS European air quality reanalysis and ground-based in-situ EEA NO$_2$ measurements. The training is organized in three sequential phases: pre-training on process-based CAMS NO$_2$, multi-constraint fine-tuning with both CAMS and EEA data, and adaptive fine-tuning to recent NO$_2$ trends. The resulting model generates daily, high-resolution (2 km × 2 km) 3D NO$_2$ fields. Arrows indicate the data flow and phased training process.**

DACNO$_2$ is developed to provide daily 3D NO$_2$ fields at high spatial resolution (2 km × 2 km) with improved accuracy and generalizability by integrating multi-source data, physically consistent process-based datasets, and real-world measurements. The overall framework, illustrated in Fig. 1, combines diverse data streams with a phased training strategy.

DACNO$_2$ uses five groups of input features: temporal indicators, emission inventories and proxies, geographic data, ERA5 single-level meteorological variables, and ERA5 multi-level meteorological variables. Together, they provide complementary information on spatial and temporal NO$_2$ variability. For model training, the targets are process-based NO$_2$ fields from the CAMS European air quality reanalyses (Inness et al., 2019; Peuch et al., 2022)

and real-world surface $NO_2$ measurements from the EEA AirBase network ~~(European Environment Agency, 2024).~~(European Environment Agency, 2024). CAMS supplies physically consistent large-scale 3D $NO_2$ distributions, while EEA data constrain the model to match local concentration patterns. Details on data preparation are provided in Section 2.2.

To effectively learn $NO_2$ patterns from diverse datasets, DACNO$_2$ employs an encoder–decoder architecture with five dedicated encoder branches, each tailored to a specific group of input features. The model structure is described in Section 2.3.

Model training is organized into three sequential phases. In Phase 1, a baseline model is pre-trained on process-based CAMS data. In Phase 2, the model is further trained with both process-based and measurement data, improving its ability to represent local $NO_2$ gradients. In Phase 3, the model is fine-tuned using recent measurements to reflect current $NO_2$ trends and support real-world applications. Details of the training approach are provided in Section 2.4.

## 2.2 Dataset Preparation

### 2.2.1 Input Features

$DACNO_2$ utilizes 38 input datasets, organized into five groups: temporal indicators, emission inventories and proxies, geography, single-level meteorology, and multi-level meteorology. Details of all input features and their sources are provided in Table 1.

The temporal indicator group consists of the day of the week and the daily number of flights. The day of the week captures regular human activity cycles, reflecting variability between weekdays and weekends. Data on the daily number of flights, aggregated for nine countries in the study area (Eurocontrol, 2025), can indicate irregular activity such as holiday periods or major events, which may help explain the irregular changes in $NO_2$ emissions. Emission inventories and proxies include anthropogenic $NO_x$ emission inventories, road density, population density, and nighttime light. These features provide direct and indirect measures of $NO_x$ emissions, with high-resolution proxies complementing inventories at finer spatial scales. All datasets are resampled to ~~a~~the 2 km grid using interpolation, averaging, or rasterization methods.

Geographic datasets include land elevation and land cover, providing terrain context to the ML model. Elevation influences atmospheric transport by creating physical barriers that can trap pollutants (Giovannini et al., 2020), while land cover serves as a proxy for the location and type of surface emissions (Beelen et al., 2013). Land cover is categorized into five classes: artificial surfaces, agricultural areas, forests and semi-natural areas, wetlands, and water bodies, aggregated from the original 44 categories by the mode method (the most frequently occurring land cover type). Both elevation and land cover data are resampled to ~~a~~the 2 km grid.

Meteorological features provide atmospheric information from the surface through the free troposphere, obtained from the European Centre for Medium-Range Weather Forecasts (ECMWF) ERA5 hourly single-level and multi-level (pressure-level) datasets (Hersbach et al., 2020). We use 24-hour meteorological features for the target day. Meteorological data are horizontally resampled to ~~a~~the 16 km grid, for three reasons: (1) the native ERA5 resolution (0.25° × 0.25°, approximately 25 km × 25 km) is coarser than 2 km × 2 km, and bilinear interpolation would mainly introduce artificial smoothness rather than genuine fine-scale gradients; (2) retaining many meteorological variables at 2 km × 2 km would impose a significant computational burden; and (3) the $DACNO_2$ architecture uses a hierarchical encoder-decoder, where upscaling and downscaling follow a factor-of-two scaling

scheme (e.g., 2 km, 4 km, 8 km, 16 km). Although the ERA5-Land data can provide higher resolution (0.1° × 0.1°, approximately 9 km × 9 km), it only covers the continental areas, which is ~~not consistent~~inconsistent with the model application scope.

The day-of-week feature is normalized using sine and cosine transforms to retain its cyclical nature. Land cover is one-hot encoded to convert categorical data into a numerical format. All other input features are normalized with z-scores, based on the mean and standard deviation of the training set.

Notably, satellite-derived $NO_2$ products were deliberately excluded from the input features for two key reasons. First, frequent data gaps in satellite products, due to cloud cover and quality control, would propagate into the model's output, preventing the generation of continuous, gap-free fields. Second, this exclusion allows for an independent evaluation of the model against satellite observations and preserves the potential to use satellite data as an independent constraint in future work.

**Table 1. Summary of inputs and training targets for the DACNO$_2$ model development.**

| Group | Data | Spatial Resolution | Temporal Resolution | Dimension | Data Source |
|---|---|---|---|---|---|
| | | Inputs | | | |
| Temporal indicator | Daily number of flights | - | Daily | 1D (time) | (Eurocontrol, 2025) |
| | Day of week | - | - | | - |
| Emission inventories and proxies | CAMS global emission inventories | Anthropogenic sector (0.1° × 0.1°) Shipping sector (0.25° × 0.25°) | - (average for 2018) | 2D (latitude × longitude) | ~~(Soulie et al., 2024)~~(Soulie et al., 2024) |
| | Road networks (five types) | Vector data | - | | Global Roads Inventory Project (GRIP) global roads database (Meijer et al., 2018) |
| | Nighttime light | 500 m × 500 m | - (average for 2019 to 2022) | | Annual global Visible Infrared Imaging Radiometer Suite (VIIRS) dataset (Elvidge et al., 2021) |
| | Population | 1 km × 1 km | - | | JRC-GEOSTAT 2018 gridded dataset (Silva et al., 2021) |
| Geography | Land elevation | 90 m × 90 m | - | | Multi-Error-Removed Improved-Terrain digital elevation models (MERIT DEM) (Yamazaki et al., 2017) |
| | Land cover (resampled to 5 classes via mode aggregation) | ~~100m~~100 m × 100 m | - | | Coordination of Information on the Environment (CORINE) Land Cover 2018 (Feranec et al., 2016) |
| Meteorology | Boundary layer height<br>Mean boundary layer dissipation<br>Surface pressure<br>Dewpoint Temperature<br>2m Temperature<br>10 m U and V wind<br>Leaf area index (for low and high vegetation) | 0.25° × 0.25° | Hourly | 3D (latitude × longitude × time) | European Center for Medium-Range Weather Forecasts (ECMWF) ERA5 hourly time-series data on a single ~~levels~~level from 1940 to the present (Hersbach et al., 2020) |

| | | | | | |
|---|---|---|---|---|---|
| | Mean evaporation rate<br>Mean snow rate<br>Mean surface net radiation flux (short and long wave)<br>Mean total precipitation rate | | | | |
| | Geopotential<br>Vorticity<br>Relative humidity<br>Temperature<br>U and V wind<br>Vertical velocity | 0.25° × 0.25°<br>8 layers from 1000 hPa to 550 hPa | | 4D (latitude × longitude × height × time) | ECMWF ERA5 hourly data on pressure levels from 1940 to the present |
| Training targets | | | | | |
| Process-based data | CAMS European air quality reanalysis $NO_2$ | 0.1° × 0.1°<br>8 layers from the surface to 5000 m | Daily (average from hourly) | 3D (latitude × longitude × height) | (Peuch et al., 2022; Inness et al., 2019) |
| Surface measurements | EEA AirBase surface $NO_2$ | - | Hourly | 2D (latitude × longitude) | EEA AirBase network ~~(European Environment Agency, 2024)~~(European Environment Agency, 2024) |

### 2.2.2 Training Targets

The training targets include CAMS European air quality reanalysis profile data (CAMS $NO_2$) and in-situ measurements from the EEA AirBase network (EEA $NO_2$). The datasets are both listed in Table 1. CAMS $NO_2$ offers extensive and continuous 3D $NO_2$ data aligned with physical and chemical processes, while EEA $NO_2$ provides ground-based in-situ measurements from sparsely distributed monitoring stations.

CAMS $NO_2$ is the median ensemble of 11 different regional models (Inness et al., 2019; Peuch et al., 2022). The dataset provides hourly $NO_2$ distributions at eight vertical heights above the surface (surface, 50m, 100m, 250m, 500m, 750m, 1000m, 2000m, 3000m, and 5000m) and has a horizontal resolution of 0.1° × 0.1° (10 km × 10 km). CAMS $NO_2$ has assimilated EEA observations and includes both interim and validated reanalyses. Interim data relies on near-real-time observations without full validation, whereas validated data undergo rigorous quality control with an additional delay. In this study, we used CAMS $NO_2$ data from 2019 to 2023, where the 2019–2021

data are validated reanalysis data and the 2022–2023 data are interim reanalysis data, based on data availability. CAMS $NO_2$ was processed by averaging hourly data to daily values and by bilinearly interpolating its horizontal resolution from 10 km to 8 km to match the model's factor-of-two scaling scheme. This regridding is used for grid alignment only and supports the computation of the loss function during training. In addition, CAMS $NO_2$ concentrations at each vertical ~~level~~layer were rescaled by ~~multiplying~~dividing them by the ~~inverse of the~~ ratio ~~between~~of the mean $NO_2$ concentration at that ~~level and~~layer to the mean surface-~~level~~layer $NO_2$ concentration, where ~~the~~this ratio was calculated from the training dataset. This adjustment ensures that the model gives adequate attention to higher-altitude $NO_2$ concentrations, which are otherwise much lower than surface values and could be neglected during training (Li and Xing, 2024; Kuhn et al., 2024a). During model inference, the predicted $NO_2$ concentrations at each ~~level~~layer were multiplied by the corresponding ratio to restore the original vertical profile.

EEA $NO_2$ was collected from background and industrial monitoring stations ~~(European Environment Agency, 2024)~~(European Environment Agency, 2024) and mapped onto ~~a 2 km grid. Traffic stations were excluded because their measurements represent a very local area, significantly smaller than the 2 km grid cells of our study.~~the 2 km grid. Such stations have spatial representativeness of several to dozens of square kilometers, enabling cover our target grid size. However, traffic stations were excluded because their measurements represent a very local area (< 1 $km^2$), significantly smaller than the 2 km grid cells of our study (Kracht et al., 2017). If multiple stations were located within the same grid cell, their values were averaged. When both background and industrial stations existed in a grid cell, the cell was classified as background. The stations with at least 20% effective observations per year are selected. In total, ~~773~~748 grid cells with measurements were identified, with 575 assigned for training and ~~198~~173 for final evaluation. Because background EEA $NO_2$ is assimilated into CAMS, the split of background stations followed the CAMS model assimilation system (Copernicus Atmosphere Monitoring Service, 2024) to prevent data leakage, while industrial stations were randomly split. All EEA $NO_2$ data were converted from hourly to daily averages. The spatial distribution of training and evaluation stations is shown in Fig. S1, along with the distribution density and the average surface $NO_2$ concentration map. It is important to note that some in-situ $NO_2$ measurements can be biased positively. This occurs because chemiluminescence instruments equipped with heated molybdenum converters can partially convert other reactive nitrogen species ($NO_z$, such as peroxyacetyl nitrate (PAN) and $HNO_3$) and misreport them as $NO_2$. This introduces $NO_y$ bias into the EEA measurements (Lamsal et al., 2008; Villena et al., 2012). To address this issue in future research, one potential approach is to use chemical model simulations, such as WRF-Chem, to estimate this interference and adjust the affected monitoring stations (Kuhn et al., 2024a).

### 2.2.3 Patch-Based Data Processing and Reconstruction

To balance the model's receptive field and computational efficiency, we used a patching method~~.~~ because training and inference on the full domain on the 2 km grid as a single sample is not feasible, given the multi-branch 2D and 3D inputs and the 3D decoder. Specifically, all datasets except the temporal indicator were divided into patches of 512 km × 512 km with partial overlap. This produced grid sizes of 32 × 32 for ERA5 meteorological data, 64 × 64 for CAMS $NO_2$ data, and 256 × 256 for emission inventories and proxies, geographic data, and EEA $NO_2$ data. The patch size retains regional spatial context relevant for $NO_2$ variability while remaining compatible with the factor-of-two scaling scheme used in the encoder–decoder. Partial overlapping is used to reduce boundary effects because predictions near patch edges have reduced spatial context, and overlapping patches ensure each grid cell is predicted from at least one patch interior. In this study, each patch was treated as a single input sample ~~for the model~~, and the stride was set to generate 12 overlapping samples ~~were generated for one~~ per day~~.~~, covering the full domain while keeping the daily sample count computationally manageable. More samples can be generated as needed by reducing the stride of the sliding window. Additionally, if targeting higher resolution (e.g., 1 km × 1 km or 500 m × 500 m), larger patches are required, resulting in an exponential increase in computational cost.

During model inference, the output patches were merged using a weighted averaging scheme based on a 2D Hann window (Oppenheim, 1999), which assigns lower weights to patch edges and higher weights to central regions. For each grid cell, weighted values from all overlapping patches were summed and normalized by the total weights. This reconstruction method reduced edge artifacts in overlapping areas and ensured smooth transitions across patch boundaries.

### 2.3 Model Architecture and Design

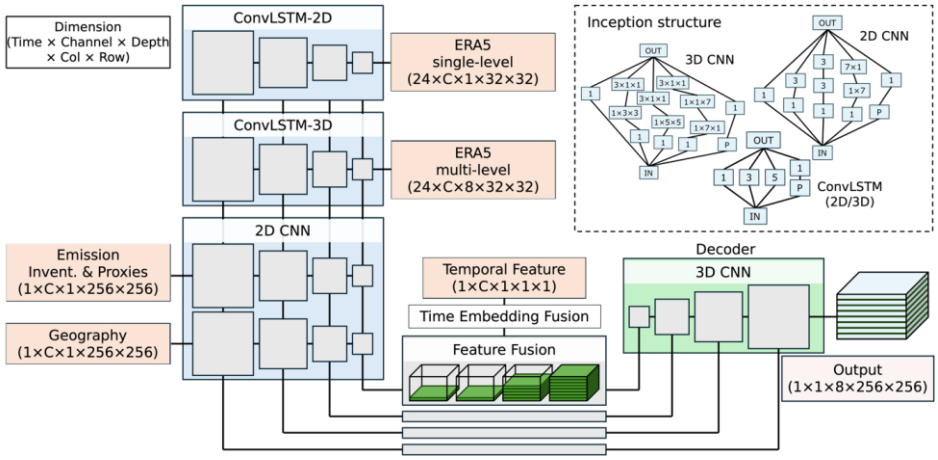


**Figure 2. DACNO$_2$ model architecture. The model features a multi-branch encoder–decoder design for daily 3D NO$_2$ prediction. Five input groups are processed separately: ERA5 single-level meteorological variables (ConvLSTM-2D), ERA5 multi-level meteorological variables (ConvLSTM-3D), emission inventories and proxies (2D CNN), geography (2D CNN), and temporal features (MLP-based embedding fusion). Outputs from all encoder branches are fused and passed into a unified 3D CNN decoder to generate high-resolution NO$_2$ fields. The architecture enables the extraction of spatial, temporal, and multi-level atmospheric features, supporting fine-scale NO$_2$ modeling. Input and output dimensions are indicated for each module.**

The architecture of the DACNO$_2$ model is illustrated in Fig. 2. The model adopts an encoder–decoder framework with residual connections (He et al., 2016) to map multi-source input features to the daily 3D NO$_2$ field. The residual connections pass intermediate feature maps from the encoder directly to matching decoder stages, which helps retain fine-scale information across the upscaling path and improves training stability. DACNO$_2$ integrates several types of neural network modules, including multilayer perceptron (MLP), convolutional neural network (CNN), and convolutional long short-term memory (ConvLSTM), to process and fuse heterogeneous input tensors. Each module is chosen for its specific strengths in handling different data structures. ConvLSTM is for spatiotemporal sequences, CNN is for spatial hierarchies, and MLP is for tabular feature vectors. Inception-style structures are applied in several neural network modules to enable the model to capture both local-scale and broader-scale spatial features.

### 2.3.1 Encoder and Decoder

DACNO$_2$ encodes ERA5 single-level (hourly 2D) and multi-level (hourly 3D) meteorological data using ConvLSTM-2D and ConvLSTM-3D modules, respectively. Both modules are based on the ConvLSTM architecture proposed by Shi et al. (2015), which combines convolutional layers for spatial feature extraction with long short-term memory (LSTM) units for temporal sequence modeling. LSTM units use gated memory to retain information from earlier time steps (Hochreiter and Schmidhuber, 1997), so the ConvLSTM branches can learn day-scale meteorological evolution rather than treating each hour independently. ERA5 data are processed using a progressive upscaling strategy, where the horizontal grid size increases stepwise from 32 × 32 to 64 × 64, 128 × 128, and 256 × 256, while the vertical dimension remains at 8 for multi-level inputs. This upscaling preserves spatial detail and enables residual connections to the decoder, unlike conventional encoders that downsample feature maps. To manage computational cost, the temporal sequence length is halved after each ConvLSTM block through subsampling, resulting in sequence lengths of 24, 12, 6, and 3 at successive stages. At each stage, the last time slice is extracted for feature fusion.

Emission and geographic variables are encoded by dedicated 2D CNN blocks, which extract hierarchical spatial features as the resolution decreases from 256 × 256 to 32 × 32. At the 32 × 32 latent stage, features from all four branches are passed through CNN-based transition layers, each forming a 3D tensor. The latent space represents a compressed internal representation where all encoder branches are mapped onto a common 3D tensor before the decoder reconstructs the 2 km × 2 km output fields. For each branch, feature values are assigned only to physically relevant vertical ~~levels~~layers within the tensor, while all other ~~levels~~layers are set to zero. Specifically, emission and geographic features are assigned to the surface ~~level~~layer, ERA5 single-level features are placed in the lowest five ~~levels~~layers, and ERA5 multi-level features span all vertical ~~levels~~layers. The resulting tensors are concatenated along the channel dimension and fused using a 3D CNN block. Temporal indicators are encoded by an MLP, then expanded to match the latent spatial dimensions, and integrated at this stage, allowing the model to capture both spatial and temporal context. The same feature fusion scheme is applied to residual connections between the encoder and decoder ~~at~~across multiple spatial scales, although temporal embedding is used only at the 32 × 32 stage.

The decoder uses 3D CNN modules with hierarchical upscaling from 32 × 32 to 256 × 256 in the horizontal dimension, while maintaining a vertical size of 8. This structure learns spatial correlations across multiple altitude ~~levels~~layers and captures both horizontal and vertical dependencies in $NO_2$ distributions. All 2D and 3D CNN

blocks use the sigmoid linear unit (SiLU) activation function (Elfwing et al., 2017), while the output layer uses the softplus activation function to ensure non-negative estimates of the 3D $NO_2$ field.

### 2.3.2 Inception-Based Modules

To enhance multi-scale feature extraction, DACNO$_2$ incorporates inception modules throughout its architecture (Fig. 2), inspired by the work of inception architecture (Szegedy et al., 2014; Szegedy et al., 2015). ~~The core concept of this architecture is to use parallel.~~ Each inception module runs multiple convolutional ~~operations~~paths with ~~varying~~different kernel sizes~~, enabling the model to efficiently~~ in parallel and concatenates their outputs, so DACNO$_2$ can capture both ~~fine-scale and broad features simultaneously~~local gradients and broader regional structure within the same layer. In the ConvLSTM-2D and ConvLSTM-3D branches, each inception block applies parallel convolutional operations with varying kernel sizes (1~~×~~ × 1, 3~~×~~ × 3, 5~~×~~ × 5) and a max-pooling branch, enabling the model to capture both local and broader spatiotemporal patterns. The max-pooling branch performs spatial downsampling by taking local maxima, which provides a coarse-scale summary that complements the convolution branches and improves multi-scale feature extraction. The 2D CNN modules extend this approach, combining parallel 1~~×~~ × 1, 3~~×~~ × 3, and 5~~×~~ × 5 convolutions, a factorized 7~~×~~ × 7 path (decomposed into 1~~×~~ × 7 and 7~~×~~ × 1 convolutions), and a pooling branch. For 3D CNN modules, inception blocks use parallel convolutions with different spatial and vertical kernel shapes, such as 1~~×1×1, 1×3×3, and 3×1×1, along with a pooling branch. In all cases, each parallel branch includes its own batch normalization, activation, and dropout, after which the outputs are concatenated along the channel dimension.~~ × 1 × 1, 1 × 3 × 3, and 3 × 1 × 1, along with a pooling branch. In all cases, each parallel branch includes its own batch normalization, activation, and dropout, after which the outputs are concatenated along the channel dimension. Batch normalization normalizes intermediate activations within each mini-batch, reducing sensitivity to feature scaling and often improving optimization behavior (Ioffe and Szegedy, 2015). Dropout randomly masks a fraction of activations during training, which reduces overfitting and helps generalization when training on heterogeneous inputs (Srivastava et al., 2014). A similar design has been applied in a previous deep learning model for $NO_2$ estimation (Zhang et al., 2022a). It enables the model to effectively integrate information across multiple spatial and vertical scales, improving the representation of complex atmospheric $NO_2$ distributions.

## 2.4 Three-Phase Training Strategy

The $DACNO_2$ model development employs a three-phase training strategy, including pre-training, multi-constraint fine-tuning, and adaptive fine-tuning. Such a strategy enables the model to learn general patterns (e.g., a-priori knowledge) from a broad dataset and then transfer this internal knowledge to improve its performance on a new, more specific task. Similar approaches have been widely adopted in the development of artificial intelligence (AI) models across various domains, such as earth system modeling, large language models, and biomedical image analysis (Zhuang et al., 2019; Zhou et al., 2017; Ding et al., 2023; Bodnar et al., 2024).

### 2.4.1 Phase-1

In the first phase, the $DACNO_2$ model was pre-trained on the CAMS $NO_2$ data. This dataset provides physically consistent 3D $NO_2$ distributions by assimilating real-world observations into chemical transport models (Inness et al., 2019), enabling the model to learn comprehensive 3D $NO_2$ patterns governed by broad-scale atmospheric processes. This approach is inspired by recent progress in AI weather modeling (Bi et al., 2023; Lam et al., 2023) and the earth system foundation model (Bodnar et al., 2025), which uses ERA5 and CAMS data for 3D forecasting of weather and air quality.

In this step, the training loss is defined as the sum of the Mean Squared Error (MSE) loss and the Structural Similarity Index Measure (SSIM) loss (Zhao et al., 2017; Zhou et al., 2004) between the $DACNO_2$ prediction and the CAMS $NO_2$ data ~~at~~on the 8 km ~~resolution~~grid.

$$Loss = Loss\mathrm{MSE}_{DACNO_2-CAMS} + Loss\mathrm{SSIM}_{DACNO_2-CAMS} \quad (1)$$

MSE quantifies the absolute differences in $NO_2$ concentrations, while SSIM evaluates the similarity of spatial patterns between model outputs and the CAMS reference. SSIM is computed independently at each vertical ~~level~~layer by comparing normalized 2D horizontal slices of the predicted and reference $NO_2$ fields. Specifically, each slice is min-max normalized to the range of 0 to 1 prior to SSIM calculation, ensuring that the SSIM loss reflects only structural similarity rather than magnitude differences. The final SSIM loss is calculated as one minus the mean SSIM across all vertical ~~levels~~layers. This dual-loss formulation encourages the model to match both the overall concentration values and the detailed spatial structures of 3D $NO_2$ fields.

The model was trained and validated using a random sample split from the 2019, 2021, and 2022 datasets (13,140 samples, 80% for training, 20% for validation), with 2023 reserved as an independent test set. Data from 2020

was excluded from this process because a preliminary experiment showed that its inclusion substantially degraded the model performance on the unknown period (i.e., 2022 data, which was initially held out as an independent validation year in that experiment). This might be due to the unexpectedly higher $NO_2$ concentrations above 1000 m in that year (Fig. ~~S1~~S2), which is also documented in the CAMS Evaluation and Quality Control (EQC) report (Meleux et al., 2023). While the cause remains unclear, we speculate that this anomaly is related to the substantial decrease in $NO_x$ emissions during 2020 due to the COVID-19 pandemic (Levelt et al., 2022) and not well accounted for in the CAMS model. We evaluate and discuss DACNO$_2$ performance for that special year in Section 4.4.

#### 2.4.2 Phase-2

In the second phase, we fine-tuned DACNO$_2$-Phase-1 by introducing an additional MSE constraint based on EEA $NO_2$, while maintaining the CAMS $NO_2$ constraints, as shown in Equation (2). The EEA $NO_2$ MSE was computed at the surface ~~level~~layer and only ~~for~~on the 2 km ~~grids~~grid with available EEA data

$$Loss = Loss\mathrm{MSE}_{DACNO_2-CAMS} + Loss\mathrm{SSIM}_{DACNO_2-CAMS} + Loss\mathrm{MSE}_{DACNO_2-EEA} \quad (2)$$

The EEA $NO_2$ data were split into training and validation sets using the same spatiotemporal alignment as the CAMS $NO_2$ split. Most training settings remained consistent with the first phase, except that the learning rate was reduced and the EEA $NO_2$ MSE term was added to both the training loss and the validation metric. The model checkpoint with the best validation performance was selected and is referred to as DACNO$_2$-Phase-2 for subsequent use. Although Phase-2 includes the same CAMS constraint as Phase-1, which may make Phase-1 appear redundant, we recommend retaining Phase-1. Skipping directly to Phase-2 can cause the model to overfit local EEA observations and limit its ability to learn generalizable $NO_2$ patterns from process-based data.

#### 2.4.3 Phase-3

Recent changes in air quality policies and emission technologies (Castellanos and Boersma, 2012; Wang et al., 2021; Chang et al., 2023) may introduce systematic $NO_2$ variations that are not well represented in the historical training dataset~~.~~ (Fig. S7). To ensure the DACNO$_2$ model remains adaptable to such real-world changes, we introduced a third phase. In this step, we adopted a strategy inspired by the data assimilation system in the CAMS model (Inness et al., 2019). DACNO$_2$-Phase-3 is initialized from the DACNO$_2$-Phase-2 ~~was~~weights and further fine-tuned using ~~only~~ EEA $NO_2$ data from the training stations during the test period (2023 in this study~~),~~) to ~~mimic real-world~~reflect a typical application scenario. To maintain spatial patterns learned from earlier phases, a regularization term based on SSIM was added to both the training loss and validation metric. SSIM was computed

at 8 km × 8 km resolution between predictions from the updated model and DACNO$_2$-Phase-2 (equation 3):

$$Loss = Loss\mathrm{MSE}_{DACNO_2(new)-EEA} + Loss\mathrm{SSIM}_{DACNO_2(new)-DACNO_2(Phase-2)} \quad (3)$$

This approach allows the updated model to adjust prediction magnitudes in response to new measurements while preserving spatial patterns established in previous phases, since the CAMS constraint is no longer available in Phase-3. The model checkpoint with the best validation performance was selected and is referred to as DACNO$_2$-Phase-3, which incorporates recent real-world $NO_2$ variations while retaining consistency with patterns learned during earlier training.

#### 2.4.4 Training and Implementation

DACNO$_2$ was trained and implemented in Python using PyTorch on two NVIDIA A30 GPUs. Training was performed with a batch size of 56, achieved by gradient accumulation. The first and second training phases each required approximately three weeks to complete 200 epochs on three years of data. The third training phase required about one week for 100 epochs on a single year of data. Once trained, the model generates daily $NO_2$ estimates for the whole area within minutes. Further efficiency improvements are possible through hardware upgrades or model optimization.

## 3. Assessing DACNO$_2$ Performance and Evolution

### 3.1 Model Performance Across Training Phases

**Table 2. Performance of DACNO$_2$ on the 2023 test dataset.**

| (2 km × 2 km) | DACNO$_2$-Phase-1 | | | | DACNO$_2$-Phase-2 | | | | DACNO$_2$-Phase-3 | | | | CAMS-2km | | | |
|---|---|---|---|---|---|---|---|---|---|---|---|---|---|---|---|---|
| EEA | RMSE (ug/m$^3$) | r | $R^2$ | bias (ug/m$^3$) | RMSE (ug/m$^3$) | r | $R^2$ | bias (ug/m$^3$) | RMSE (ug/m$^3$) | r | $R^2$ | bias (ug/m$^3$) | RMSE (ug/m$^3$) | r | $R^2$ | bias (ug/m$^3$) |
| Total | 5.88 | 0.75 | 0.52 | -0.93 | 5.81 | 0.79 | 0.54 | 1.67 | **4.99*** | **0.82*** | **0.66*** | **-0.38*** | 5.32 | 0.80 | 0.61 | -1.15 |
| Urban | 6.45 | 0.76 | 0.47 | -2.57 | 5.64 | 0.80 | 0.59 | **0.49*** | **5.34*** | **0.82*** | **0.64*** | -1.42 | 5.89 | 0.82 | 0.56 | -2.89 |
| ~~Suburban~~Sub-urban | 5.11 | 0.79 | 0.58 | **-0.04*** | 6.01 | 0.81 | 0.42 | 2.87 | 4.55 | 0.83 | 0.67 | 0.58 | **4.39*** | **0.84*** | **0.69*** | -0.23 |
| Rural | 5.22 | 0.76 | 0.42 | 1.96 | 5.96 | 0.76 | 0.25 | 3.17 | **4.59*** | 0.78 | **0.55*** | **1.05*** | 4.79 | **0.80*** | 0.51 | 1.98 |

| (10 km × 10 km) | DACNO$_2$-~~10km~~Phase-1 | | | | DACNO$_2$-Phase-2 | | | | DACNO$_2$-Phase-3 | | | |
|---|---|---|---|---|---|---|---|---|---|---|---|---|
| CAMS | RMSE (ug/m$^3$) | r | $R^2$ | bias (ug/m$^3$) | RMSE (ug/m$^3$) | R | $R^2$ | bias (ug/m$^3$) | RMSE (ug/m$^3$) | r | $R^2$ | bias (ug/m$^3$) |
| ~~Total levels~~All layers | **0.99*** | **0.96*** | **0.91*** | **-0.05*** | 1.17 | **0.96*** | 0.87 | 0.25 | 1.02 | 0.95 | 0.90 | -0.10 |

Inserted Cells

Inserted Cells

Deleted Cells

| | | | | | | | | | | | | |
|---|---|---|---|---|---|---|---|---|---|---|---|---|
| ~~L0~~0 m | **1.92*** | **0.94*** | **0.85*** | **-0.36*** | 2.29 | 0.93 | 0.79 | 0.75 | 1.94 | 0.93 | **0.85*** | -0.63 |
| ~~L50~~50 m | **1.58*** | **0.95*** | **0.88*** | **-0.25*** | 1.94 | 0.94 | 0.82 | 0.66 | 1.62 | 0.94 | 0.87 | -0.31 |
| ~~L250~~250 m | **1.05*** | **0.93*** | **0.83*** | 0.10 | 1.19 | **0.93*** | 0.78 | 0.41 | 1.09 | **0.93*** | 0.82 | **0.01*** |
| ~~L500~~500 m | **0.70*** | **0.92*** | **0.79*** | 0.09 | 0.71 | **0.92*** | **0.79*** | 0.16 | 0.79 | 0.90 | 0.74 | **0.05*** |
| ~~L1000~~1000 m | 0.31 | **0.89*** | 0.72 | **0.03*** | **0.30*** | **0.89*** | **0.74*** | **0.03*** | 0.39 | 0.86 | 0.56 | 0.06 |
| ~~L2000~~2000 m | **0.08*** | **0.81*** | 0.61 | -0.01 | **0.08*** | **0.81*** | **0.64*** | -0.01 | 0.09 | 0.79 | 0.48 | **0.00*** |
| ~~L3000~~3000 m | 0.04 | **0.78*** | 0.55 | -0.01 | **0.03*** | 0.77 | **0.58*** | **0.00*** | 0.04 | 0.74 | 0.40 | **0.00*** |
| ~~L5000~~5000 m | **0.01*** | **0.67*** | 0.31 | 0.00 | **0.01*** | 0.66 | **0.34*** | **0.00*** | 0.02 | 0.61 | -0.01 | **0.00*** |

*Note: For the comparison against EEA $NO_2$ (shown in the upper panel), both DACNO$_2$ outputs and CAMS $NO_2$ were evaluated ~~at~~on the 2 km ~~grids.~~grid. In this comparison, CAMS is a reanalysis product that has assimilated EEA $NO_2$ for 2023. The CAMS $NO_2$ data was interpolated to a 2 km × 2 km resolution (CAMS-2km) and used as a baseline in this comparison. For evaluating DACNO$_2$ using CAMS $NO_2$ (shown in the lower panel), DACNO$_2$ outputs were downsampled and evaluated at the original 10 km × 10 km resolution of CAMS across all vertical ~~levels~~layers as well as for individual ~~levels.~~layers. Best values within each row are highlighted in bold and marked with an asterisk (*).*

The performance of the DACNO$_2$ model was evaluated using both EEA $NO_2$ and CAMS $NO_2$ test data from 2023. For the comparison against EEA $NO_2$ (results in the upper panel of Table 2), both DACNO$_2$ outputs and CAMS

$NO_2$ were evaluated ~~at~~on the 2 km ~~grids~~grid. The CAMS $NO_2$ data was interpolated to 2- km × 2 km resolution (CAMS-2km) and served as ~~a~~the baseline ~~in~~for this comparison. The performance results were calculated across all paired measurements and model estimations. The station-specific time-series consistency analyses are provided in Fig. S3, where the results for each EEA evaluation station were calculated along the daily time-series independently. The average time-series consistency between models and EEA $NO_2$ is shown in Fig. S4. For the evaluation of $DACNO_2$ using CAMS $NO_2$ (results in the lower panel of Table 2), $DACNO_2$ outputs were evaluated at the CAMS original 10 km × 10 km resolution across all vertical ~~levels~~layers, as well as for individual ~~levels.~~layers. The layer-wise temporal correlations at the regional average and grid scales are illustrated in Fig. S6. Evaluation metrics included the root mean squared error (RMSE), Pearson correlation coefficient (r), coefficient of determination ($R^2$), and bias.

Phases 1–3 represent successive development stages of the $DACNO_2$ model. The phase-to-phase comparison in Table 2 is used to quantify the incremental effect of adding constraints and the final adaptation step. In Phase-3, the fine-tuning step uses EEA observations from the training stations in 2023. All reported EEA-based metrics are computed on the held-out evaluation stations. Comparisons with EEA $NO_2$ indicate progressive improvement across $DACNO_2$ training phases. $DACNO_2$-Phase-3 achieves the best overall agreement (RMSE = 4.99 ug/$m^3$, r = 0.82, $R^2$ = 0.66, bias = -0.38 ug/$m^3$), outperforming both $DACNO_2$-Phase-1 (RMSE = 5.88 ug/$m^3$, r = 0.75, $R^2$ = 0.52, bias = -0.93 ug/$m^3$) and $DACNO_2$-Phase-2 (RMSE = 5.81 ug/$m^3$, r = 0.79, $R^2$ = 0.54, bias = -1.67 ug/$m^3$). ~~This demonstrates the added value of incorporating local EEA constraints and adaptive fine-tuning.~~ Fig. S4 shows that the $DACNO_2$ model learns reliable temporal correlations with EEA $NO_2$ at the daily and seasonal scales since Phase-1 (r = 0.94), and these correlations are further enhanced in Phase-2 (r = 0.95) and Phase-3 (r = 0.98). This indicates that the model can represent temporal variability without using satellite $NO_2$ as an input, relying instead on meteorological and temporal indicators. Moreover, Table 2 and Fig. S4 show a positive bias for $DACNO_2$-Phase-2 in 2023. This offset is consistent with the fact that the $NO_2$ level in 2023 is lower than in the Phase-2 training years (2019, 2021, 2022), as illustrated in Fig. S7. $DACNO_2$-Phase-3 reduces the effect of the interannual variation while maintaining the temporal correlation, highlighting the role of the adaptive fine-tuning step.

Compared to the interpolated CAMS-2km dataset (RMSE = 5.32 ug/$m^3$, r = 0.80, $R^2$ = 0.61, bias = -1.15 ug/$m^3$), $DACNO_2$-Phase-3 shows improved accuracy and reduced bias. Station-type analysis further highlights the advantages of $DACNO_2$-Phase-3, especially at urban and rural sites. For urban locations, $DACNO_2$-Phase-3 achieves better agreement (RMSE = 5.34 ug/$m^3$, r = 0.82, $R^2$ = 0.64, bias = -1.42 ug/$m^3$) compared with CAMS-

2km (RMSE = 5.89 ug/m$^3$, r = 0.82, $R^2$ = 0.56, bias = -2.89 ug/m$^3$). In rural areas, DACNO$_2$-Phase-3 reduces the bias (RMSE = 4.59 ug/m$^3$, bias = 1.05 ug/m$^3$) compared to CAMS-2km (RMSE = 4.79 ug/m$^3$, bias = 1.98 ug/m$^3$). ~~These results suggest that DACNO$_2$ is more effective than CAMS at capturing localized emission patterns and small-scale spatial variability in areas with either dense emission sources or diffuse background levels~~Such improvement is consistent with station-specific time-series consistency analysis (Fig. S3). It indicates that DACNO$_2$-Phase-3 achieves station-specific Pearson correlations comparable to CAMS-2km (CAMS-2km: r-mean = 0.85, r-median = 0.88; DACNO$_2$-Phase-3: r-mean = 0.84, r-median = 0.87), while exhibiting higher station-specific $R^2$ (CAMS-2km: $R^2$-mean = 0.09, $R^2$-median = 0.52; DACNO$_2$-Phase-3: $R^2$-mean = 0.23, $R^2$-median = 0.61). The $R^2$ improvements are attributed to more high-$R^2$ sites at urban stations and fewer very low-$R^2$ sites at rural stations. The large difference between the mean and median $R^2$ is primarily caused by negative $R^2$ values at a subset of rural stations, likely due to uneven station distribution across the network and the challenge of modeling weaker, noisier signals in rural environments. Overall, these results suggest that the DACNO$_2$ model improves agreement with the independent EEA evaluation stations relative to the CAMS-2km baseline across station types. The associated spatial redistribution and localized patterns are examined explicitly in Section 3.2.

In addition, Fig. S3 shows that DACNO$_2$-Phase-3 achieves better station-specific agreement in the central domain than near the boundaries. This may be due to boundary areas that lack sufficient spatial context and have complex mountainous terrain. Additionally, a slight overestimation of DACNO$_2$-Phase-3 at EEA rural stations persists despite adaptive fine-tuning. A possible reason is the imbalance in the EEA constraint. Fig. S1 shows that most stations are located in urban and suburban areas with relatively higher NO$_2$ concentrations, whereas fewer stations are in rural areas. This may lead to positive bias in the model's estimates for rural areas, and the solutions require further investigation, including sample rebalancing strategies, expanding the study region to include more rural sites, and additional constraints. Meanwhile, given the $R^2$ definition, positive prediction bias at rural stations may be influential, as these stations generally have low NO$_2$ standard deviations and a smaller tolerance for prediction bias.

Comparisons with CAMS NO$_2$ across all ~~levels~~layers show that DACNO$_2$ effectively learns and preserves 3D NO$_2$ distributions ~~across~~through all training phases~~.~~ (Table 2). Fig. S6 further presents a layer-wise comparison between DACNO$_2$-Phase-3 and CAMS at the temporal and grid scales, showing that DACNO$_2$-Phase-3 can capture the temporal variability of NO$_2$ in 3D space. Near the surface ~~(Level 0 m),~~ DACNO$_2$-Phase-3 maintains strong agreement with CAMS (Layer 0 m: RMSE = 1.94 μg/m$^3$, r = 0.93, $R^2$ = 0.85, bias = -0.63 ug/m$^3$, Table 2),

and performance remains robust at mid-altitudes (~~Level~~Layer 500 m: RMSE = 0.79 ug/m$^3$, r = 0.90, $R^2$ = 0.74, bias = 0.05 ug/m$^3$), similar to earlier phases. However, a weak correlation is observed in the mountainous region (i.e., the Alps and the Pyrenees, Fig. S6). At higher ~~levels, particularly 5000~~ layers above 1000 m, the agreement ~~decreases, with~~in $R^2$ starts to decrease while the correlation remains stable. At 5000 m, DACNO$_2$-Phase-3 ~~yielding~~yields a near-zero $R^2$ (-0.01~~) compared to 0.31 in~~ ), which is lower than DACNO$_2$-Phase-1 (0.31) and DACNO$_2$-Phase-2 (0.34 ~~in DACNO$_2$-Phase-2. However, Pearson~~), but the correlation remains moderate ($r \geq 0.6$~~),~~ ~~indicating~~). Fig. S6 indicates that the differences between DACNO$_2$-phase-3 and CAMS at these ~~heights~~higher layers are mainly due to magnitude adjustment rather than loss of spatial structure. ~~The~~In addition, predicting very low $NO_2$ concentrations (approximately 0.~~1~~05 µg/m³ at 3000 m and 0.~~03~~02 µg/m³ at 5000 m~~; see~~, Fig. ~~S1~~S2) at ~~these~~ high ~~levels also increase relative~~layers is challenged by relatively higher noise ~~and contribute to metric variability.~~ This reduction in agreement at upper ~~levels mainly reflects the greater uncertainty and lack of direct constraints at high altitudes, which~~ layers remains a key challenge for ML-based 3D air quality modeling, which may require additional constraints from space-based observations or physical processes.

### 3.2 Model Evolution in the Multi-constraint Strategy

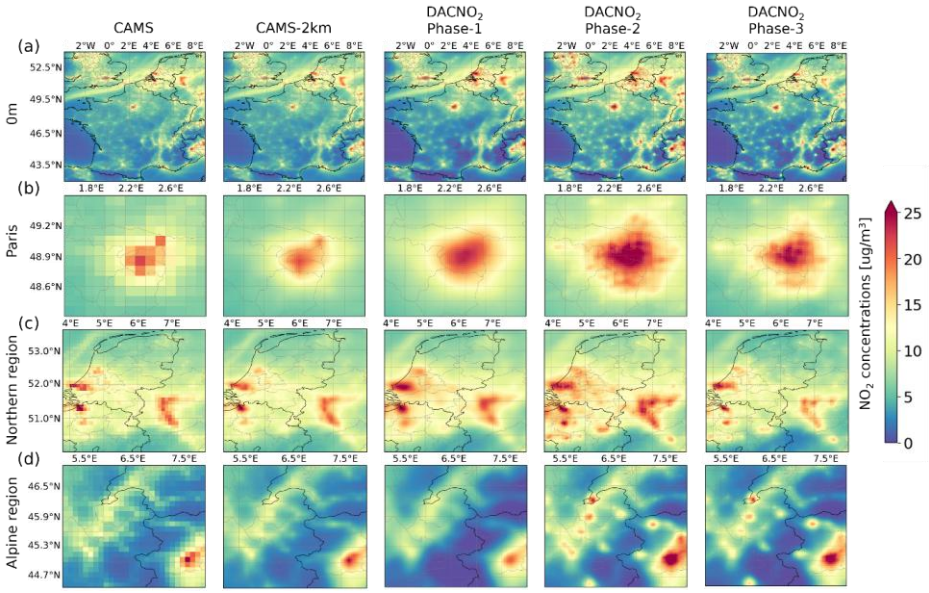


**Figure 3. Spatial comparison of surface $NO_2$ estimates for 2023 from multiple models. (a) Annual mean surface $NO_2$ fields over the entire study region from DACNO$_2$-Phase-1, DACNO$_2$-Phase-2, DACNO$_2$-Phase-3, CAMS (10 km × 10 km), and CAMS-2km (bilinearly interpolated to 2 km × 2 km). (b–d) Enlarged views for three representative local areas: (b) Paris, (c) the northern region ($NO_2$ hotspot area encompassing the Netherlands, Belgium, and the Ruhr area), and (d) the Alpine region.**

To further illustrate the evolution of estimated $NO_2$ spatial distributions achieved through a phased training, multi-constraint strategy, Fig. 3 compares average surface $NO_2$ estimates for 2023 from DACNO$_2$-Phase-1, DACNO$_2$-Phase-2, DACNO$_2$-Phase-3, CAMS, and CAMS-2km. Results are shown for the full study region and three representative local areas of Paris, the northern region ($NO_2$ hotspot area encompassing the Netherlands, Belgium, and the Ruhr area), and the Alpine region.

Across the study region (Fig. 3a), all models exhibit broad and similar $NO_2$ patterns over land and ocean, consistent with the high spatial agreement between DACNO$_2$ and CAMS $NO_2$ reported in Section 3.1.

Nonetheless, DACNO$_2$-Phase-2 and DACNO$_2$-Phase-3 yield sharper spatial contrasts and more clearly defined local NO$_2$ hotspots than CAMS and DACNO$_2$-Phase-1. As an additional experiment, we trained the model using only EEA NO$_2$ data, resulting in the DACNO$_2$-onlyobs version. As shown in Fig. ~~S2~~S8, this model yields effective NO$_2$ estimates primarily limited to the land surface and cannot reproduce the shipping track patterns, which are visible in the CAMS and DACNO$_2$ results. Meanwhile, this model produces obvious artifacts over the ocean and at higher altitudes due to the lack of training constraints. These differences highlight the significance of the CAMS NO$_2$ constraint in facilitating broad spatial generalization in ML-based models.

Differences between models become more pronounced when focusing on local regions (Figs. 3b–d). CAMS NO$_2$ exhibits visible pixelation effects in these areas due to its coarse native resolution. While bilinear interpolation (as in CAMS-2km) can smooth these effects, it does not introduce additional spatial detail, resulting in oversmoothed patterns. DACNO$_2$-Phase-1 shows a spatial NO$_2$ distribution similar to CAMS-2km, despite using high-resolution input features from emission proxies and geography. This indicates that constraints from CAMS NO$_2$ alone are insufficient for the model to capture fine-scale local NO$_2$ variability. Incorporating the EEA NO$_2$ constraint in DACNO$_2$-Phase-2 addresses this limitation, inspired by approaches in recent ML-based high-resolution surface NO$_2$ modeling studies using ground measurements as targets (Sun et al., 2024; Wei et al., 2022; Kim et al., 2021; Ghahremanloo et al., 2023). DACNO$_2$-Phase-2 reconstructs spatial patterns of NO$_2$ that better match urban layout in Paris (Fig. 3b), identifies more small-scale emission hotspots in the northern region (Fig. 3c), and enhances hotspot signals in the Alpine region (Fig. 3d). DACNO$_2$-Phase-3 retains these spatial characteristics and primarily adjusts concentration magnitudes by assimilating new measurements to better represent actual NO$_2$ levels during the application period. For example, the average surface NO$_2$ concentration estimate in Paris decreases from 11.89 μg/m$^3$ in DACNO$_2$-Phase-2 to 10.08 μg/m$^3$ in DACNO$_2$-Phase-3. This evolution demonstrates the value of integrating multiple constraints and adaptive fine-tuning for high-resolution NO$_2$ estimation.

### 3.3 Global and Local Differences Between DACNO$_2$ and CAMS

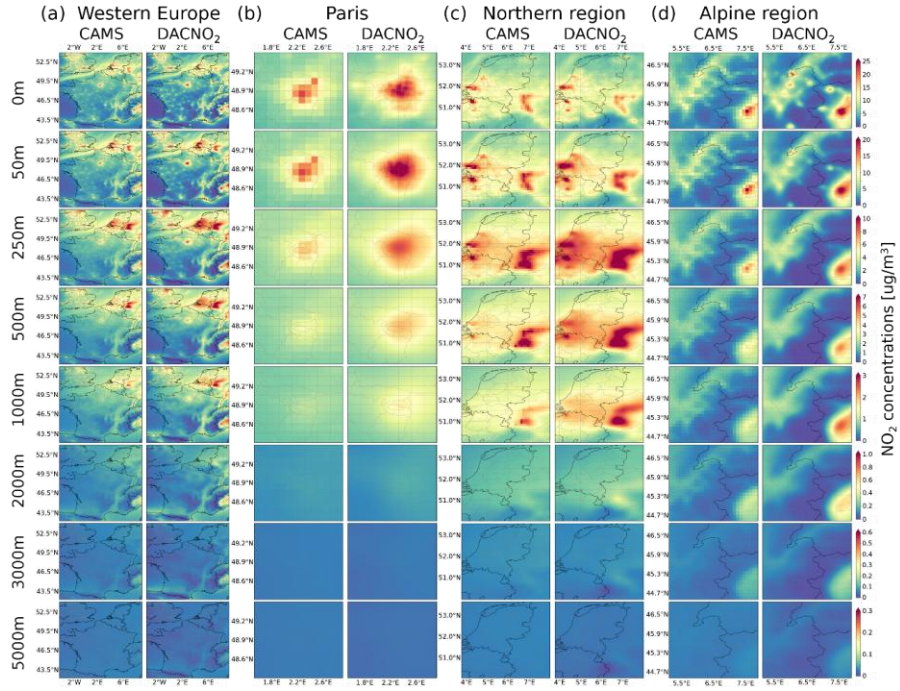


**Figure 4. Annual mean NO$_2$ distributions for 2023 estimated from DACNO$_2$-Phase-3 (2 km × 2 km) and CAMS (10 km × 10 km) at multiple vertical ~~levels. Level~~layers. Layer-wise average NO$_2$ distributions over (a) Western Europe (entire study region), (b) Paris, (c) the northern region, and (d) the Alpine region.**

To further analyze differences in 3D NO$_2$ estimates between DACNO$_2$ and CAMS, Fig. 4 compares their annual average NO$_2$ distributions for 2023 across all vertical ~~levels~~layers over the entire study region and three selected local areas. At the regional scale (Fig. 4a), DACNO$_2$ and CAMS show strong overall agreement at all altitudes, demonstrating that DACNO$_2$ effectively learns and reproduces large-scale 3D NO$_2$ structures from CAMS. However, DACNO$_2$ provides enhanced spatial detail, presenting sharper gradients and better-defined urban and industrial hotspots, particularly from the surface up to 250 m. At higher altitudes, the differences between the two

models gradually diminish, accompanied by a decrease in $NO_2$ concentrations. Nevertheless, subtle magnitude discrepancies persist, with $DACNO_2$ estimates reaching lower values, sometimes approaching zero.

Local-scale comparisons further highlight the advantages of $DACNO_2$ (Figs. 4b–d). In the Paris region (Fig. 4b), $DACNO_2$ provides finer spatial detail and stronger $NO_2$ signals at lower altitudes (e.g., 0 m: 10.08 $\mu g/m^3$; 50 m: 8.94 $\mu g/m^3$; 250 m: 4.65 $\mu g/m^3$), whereas CAMS results remain coarser with generally lower estimates (0 m: 8.43 $\mu g/m^3$; 50 m: 7.15 $\mu g/m^3$; 250 m: 3.63 $\mu g/m^3$). In the northern region (Fig. 4c), $DACNO_2$ more distinctly resolves localized emission sources at low ~~levels~~layers, capturing a greater number of hotspots than CAMS. As a result, the average $NO_2$ concentration from $DACNO_2$ is elevated throughout the boundary layer (up to 1000 m), with mean values 8.8% higher than those from CAMS. In the Alpine region (Fig. 4d), $DACNO_2$ more effectively represents terrain-driven gradients and captures $NO_2$ signals within mountainous areas, demonstrating greater sensitivity to complex topographic influences. At higher altitudes, fine-scale variability diminishes in both models and their predicted $NO_2$ fields become more similar. This is because the influence of local emissions and surface features weakens, while regional-scale processes and long-range transport dominate (see Section 4.1). This reduced difference is also accompanied by much lower $NO_2$ concentrations at higher altitudes.

## 4. Insights and Implications of DACNO₂

### 4.1 Feature Importance and Data-driven Insights

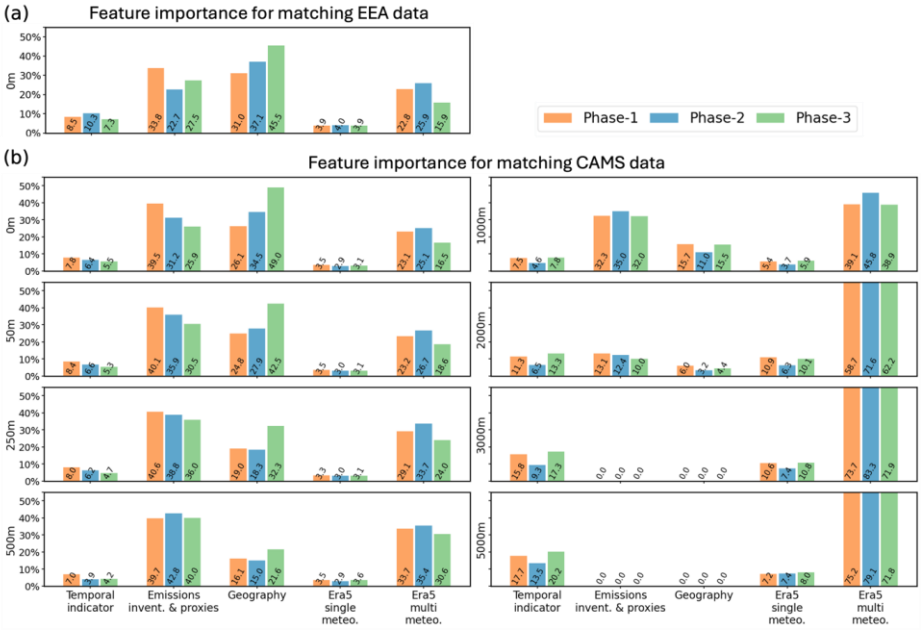


**Figure 5. Relative importance of each input feature group for DACNO₂ model predictions, evaluated using the integrated gradients (IG) method. (a) Feature group contributions to RMSE between DACNO₂ surface $NO_2$ estimates and EEA ground-based measurements for 2023. (b) Feature group contributions to RMSE between DACNO₂ and CAMS $NO_2$ estimates at different vertical ~~levels~~layers for 2023. The five feature groups are: temporal indicators, emission inventories and proxies, geography, ERA5 single-level meteorology, and ERA5 multi-level meteorology. Results are shown for each model training phase (Phase-1, Phase-2, and Phase-3), illustrating how the relative influence of input feature groups varies with training constraints and altitude. See Figure ~~S3~~S9 for the contributions of individual features within each group.**

We assessed the relative importance of input feature groups in DACNO₂ using the integrated gradients (IG) method (Sundararajan et al., 2017) implemented via the Captum interpretability library ~~(Kokhlikyan et al., 2020)~~(Kokhlikyan et al., 2020). IG quantifies the effect of varying each input feature from a zero baseline to its actual value on a selected target function. In this analysis, we computed IG at two targets: (1) the RMSE between DACNO₂ predictions and 2023 EEA $NO_2$ training measurements at the surface, and (2) the RMSE between

DACNO$_2$ predictions and 2023 CAMS NO$_2$ at multiple vertical ~~levels~~layers. Feature group results are shown in Fig. 5, and results for individual features are provided in Fig. ~~S3~~S9.

For surface NO$_2$ predictions evaluated against EEA measurements, DACNO$_2$ relies primarily on emission proxies, geographic features, and multi-level meteorological variables, while temporal indicators and single-level meteorological features play a lesser role. The addition of the EEA NO$_2$ constraint in Phase-2 and Phase-3 increases the importance of geographic data, highlighting its value for high-resolution surface NO$_2$ estimation. As shown in Fig. ~~S3~~S9, land cover emerges as the most influential single feature (36.6%) in DACNO$_2$-Phase-3~~, accounting for 36.6% of the total importance.~~. Multi-level meteorological variables dominate the meteorological contribution, ~~although the radiation variable from the single-level meteorology group also remains relevant (1.0% in Phase-3, Fig. S3). This likely reflects some~~suggesting partial redundancy between single-level and multi-level meteorological ~~features, with multi-level data providing more comprehensive atmospheric information~~inputs.

For NO$_2$ estimates by ~~level~~layer evaluated against CAMS, the distribution of input feature importance at lower ~~levels~~layers (up to 1000 m) is similar to that for surface NO$_2$ evaluated against EEA, suggesting that DACNO$_2$ remains relatively stable across training phases with different constraints. Differences between the three-phase models are most apparent near the surface but gradually diminish with height. The importance of geographic features steadily decreases ~~as~~with height ~~increases, while~~, whereas emission features reach their ~~highest~~strongest influence ~~around~~at approximately 500 m before declining. Above 3000 m, both become negligible, reflecting the transition from the Planetary Boundary Layer (PBL), which is influenced by local surface features, into the free troposphere, which is dominated by broad-scale processes.

In contrast, temporal indicators, single-level ~~meteorology~~meteorological features, and especially multi-level meteorological features become increasingly important with height. ~~For example, in DACNO$_2$-Phase-3, the contribution from multi-level meteorology rises from 16.5% at the surface to 71.8% at 5000 m, while temporal indicators and single-level meteorology also show steady increases.~~ This shift highlights the greater reliance on temporal and large-scale atmospheric information for NO$_2$ estimates at higher ~~levels~~layers. Among these features, radiation flux ~~(3.3% at is~~3000 m, 2.4% at 5000 m) primarily drives the ~~increase in~~most important single-level ~~meteorology, while~~ meteorological variable, and wind ~~becomes~~is the dominant variable among all meteorological features (~~approximately 21% at both 3000 m and 5000 m,~~ Fig. ~~S3~~S9). Given the consistently low overall

contribution of single-level meteorological variables, future model development may consider reducing or refining the use of this feature group to streamline the input space.

Overall, the DACNO$_2$ model is developed by combining multi-scale inputs and multi-source constraints. The fine-scale spatial structure on the 2 km grid is primarily informed by high-resolution emission-related proxies and geographic features, whereas large-scale spatiotemporal variation and vertical structure are driven by meteorological variables and temporal indicators. Through the phased training strategy, the CAMS constraint transfers large-scale spatiotemporal variation to the DACNO$_2$ model, and the EEA constraint guides the model to use fine-scale static inputs to shape this variation on the 2 km grid spatially.

595 **4.2 Enhanced Vertical $NO_2$ Profile Representation**

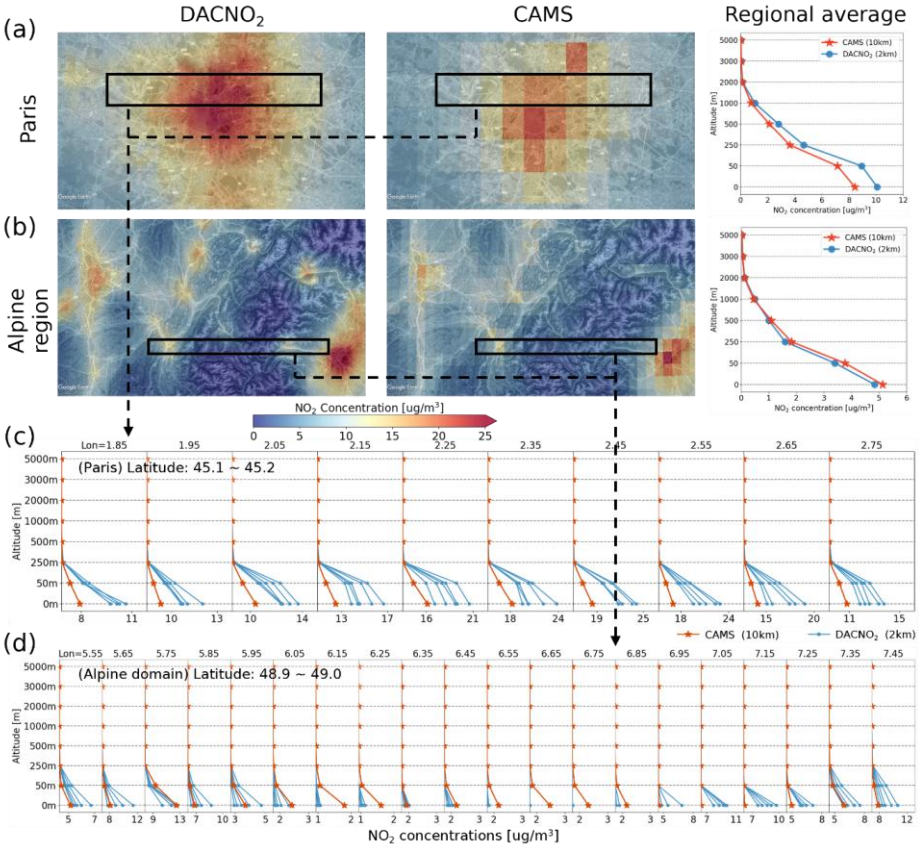


**Figure 6. Comparison of $NO_2$ profile estimates from DACNO$_2$-Phase-3 (2 km ~~resolution~~× 2 km) and CAMS (10 km ~~resolution~~× 10 km) for the Paris and Alpine regions in 2023. Regional average vertical profiles and surface $NO_2$ distributions for Paris (a) and the Alpine region (b), with results shown over © Google Earth imagery. Interpixel** 600 **variability of $NO_2$ profiles from DACNO$_2$ and CAMS along a 100 km transect (black boxes) in the Paris area (c) and a 200 km transect in the Alpine region (d), illustrating local-scale differences in vertical structure.**

Fig. 6 compares the average 2023 $NO_2$ profile estimates from DACNO$_2$-Phase-3 (2 km × 2 km) and CAMS (10 km × 10 km) for the Paris and Alpine regions, with results overlaid on Google Earth imagery for geographic

context. In Paris, the regional average profile (Fig. 6a) indicates that DACNO$_2$ yields higher ~~near-surface~~ NO$_2$ concentrations up to 2000 m and steeper vertical gradients compared to CAMS. This enhancement likely results from DACNO$_2$'s use of high-resolution emission proxies and land cover information, allowing the model to resolve smaller and more localized emission sources (Kuik et al., 2018; Shahrokhishahraki et al., 2022). At the local scale, we take a transect over the grids of 100 km over Paris to compare the interpixel profile variability from CAMS ~~(10 km)~~ and DACNO$_2$ (~~2 km) (~~Fig. 6c). It is observed that DACNO$_2$ more clearly distinguishes spatial variability in the vertical structure, showing sharper contrasts and more pronounced local peaks than CAMS, particularly below 250 m. The regional average profiles for the Alpine area are similar between DACNO$_2$ and CAMS (Fig. 6b), which is due to the overall lower concentrations over this region with limited emission sources. However, local differences remain visible across a 200 km transect (Fig. 6d). DACNO$_2$ captures higher NO$_2$ concentrations around urban and small-scale hotspots, especially in valleys and canyons where pollutants tend to accumulate. Conversely, DACNO$_2$ provides lower NO$_2$ estimates in areas between the mountains with few sources. Overall, DACNO$_2$ provides more spatially detailed 3D NO$_2$ fields, revealing greater variability in the vertical profiles across different grids in this complex terrain. This refinement is important, as small point and line sources can contribute significant NO$_2$ in mountainous regions (Kim et al., 2021).

To assess how vertical profiles differ between the two models across environments, we analyzed the mean DACNO$_2$-to-CAMS profile ratio across the entire study region in urban, suburban, rural, and uninhabited environments classified based on population density (Fig. S10) and the urbanization definition (Dijkstra et al., 2021). The results indicate that the DACNO$_2$-Phase-3 adjustment is not a uniform scaling of the CAMS field. Instead, near the surface, DACNO$_2$-Phase-3 shows higher concentrations relative to CAMS in urban regions (about 6%) and lower concentrations in other areas (from about -20% to -1%). In the boundary layer (1000 m), the NO$_2$ concentrations are systematically higher in DACNO$_2$-Phase-3 compared to CAMS (from 10% to 30%), except in the uninhabited area (remains the same). At higher layers, DACNO$_2$-Phase-3 values converge to a lower ratio (about -22% to -15%) at 5000 m for the entire region. This behavior is also reflected in the layer-integrated column diagnostics shown in Fig. S11, which indicate near preservation of the regional column (0 – 5000 m), accompanied by a significant redistribution in the lower (0 – 1000 m) and conservative adjustment in upper (1000 – 5000 m) layers. Together, these results suggest that the DACNO$_2$-Phase-3 primarily redistributes NO$_2$ within the lower layers, enhancing horizontal contrast linked to human activity and emission strength, while maintaining consistently low estimates in the upper layers.

Additionally, we assessed the profile ratio across the three phases (Fig. S10). The results indicate that applying EEA constraints almost systematically increases NO$_2$ estimates in DACNO$_2$-Phase-2 relative to DACNO$_2$-Phase-1, likely because the CAMS data used for pretraining in Phase-1 underestimates NO$_2$ at EEA measurement stations. In contrast, the EEA constraint reduces NO$_2$ estimates in DACNO$_2$-Phase 3 relative to DACNO$_2$-Phase-2, consistent with the lower surface NO$_2$ levels observed in 2023 compared with the training years (2019, 2021, 2022, Fig. S7). However, the boundary-layer NO$_2$ estimates exhibit different trends that do not align with phase-dependent changes, which warrants further investigation.

In this work, the vertical structure of DACNO$_2$ is assessed through comparison with CAMS. Independent evaluation against vertically resolved observations, such as MAX-DOAS or aircraft measurements, would be the next step in future work. Such an analysis would require an hourly version of the DACNO$_2$ fields to provide daytime data and the application of appropriate observation operators to ensure comparability between the model and the observational data.

### 4.3 Implications for Satellite $NO_2$ Retrievals

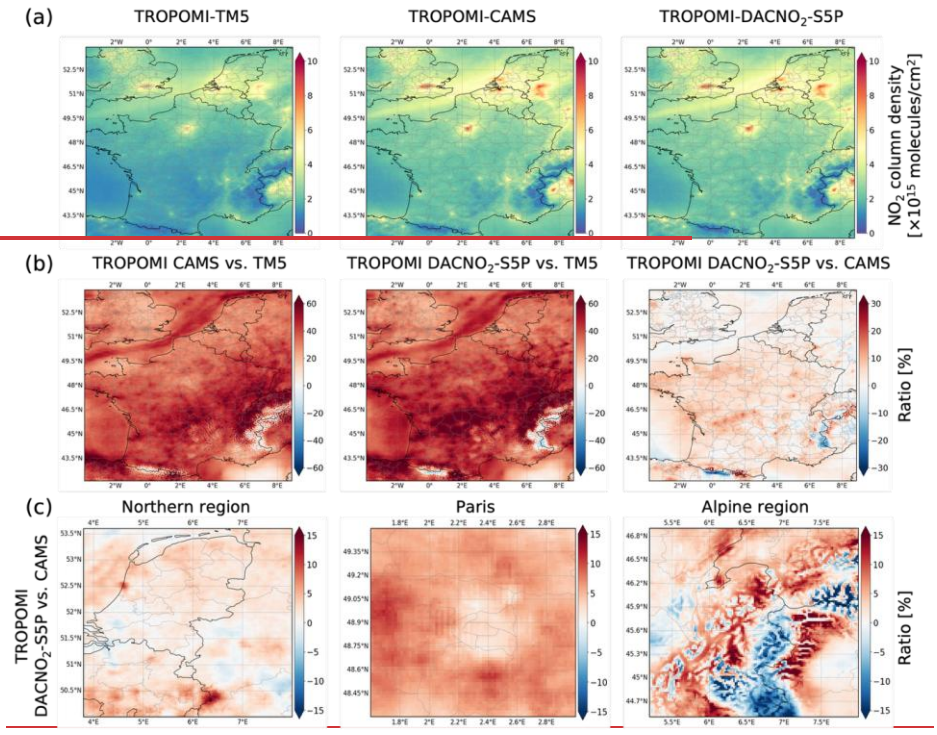

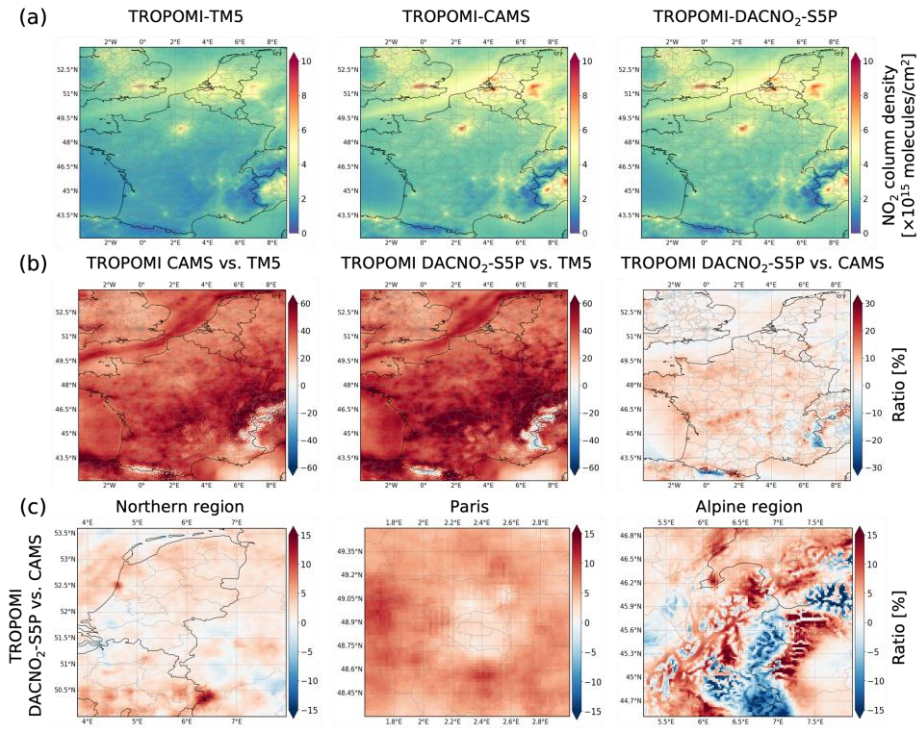


**Figure 7. Impact of a-priori profile selection on TROPOMI tropospheric $NO_2$ column retrievals for 2023. (a) Annual mean TROPOMI $NO_2$ columns retrieved using the original TM5 (~~about~~1° × 1°, approximately 100 km × 100 km), CAMS-S5P (10 km × 10 km), and $DACNO_2$-S5P (2 km × 2 km) a-priori profiles. (b) Spatial distribution of the relative difference (%) in TROPOMI $NO_2$ columns retrieved with three profiles. (c) The relative change in retrieved $NO_2$ columns across three subregions (the northern region, Paris, and the Alpine region) when using $DACNO_2$-S5P versus CAMS-S5P profiles.**

To assess the potential of $DACNO_2$ for satellite $NO_2$ product improvement and development, we tested its use as a source of a-priori $NO_2$ profiles in TROPOMI retrievals. For this, a dedicated version of the model ($DACNO_2$-S5P) was developed for the TROPOMI overpass time, predicting a 3-hour average $NO_2$ (11:00–13:00 UTC) using the same three-phase strategy. The model targets, named CAMS-S5P and EEA-S5P, represent process-based and measured $NO_2$ data during this period.

Model evaluation (Table S1) shows DACNO$_2$-S5P agrees well with CAMS-S5P (RMSE = 0.98 µg/m$^3$, r = 0.94, $R^2$ = 0.88, bias = 0.03 µg/m$^3$) ~~at~~on the 10 km ~~grids~~grid. Compared to EEA-S5P measurements, DACNO$_2$-S5P achieves better agreement (RMSE = 5.07 µg/m$^3$, r = 0.77, $R^2$ = 0.59, bias = 0.05 µg/m$^3$) than CAMS-S5P (RMSE = 5.27 µg/m$^3$, r = 0.76, $R^2$ = 0.55, bias = -0.94 µg/m$^3$).

We replaced the original TM5 a-priori profiles (~~about~~1° × 1°, approximately 100 km ~~resolution~~× 100 km) in the TROPOMI retrievals with CAMS-S5P and DACNO$_2$-S5P profiles, following the approach described in Douros et al. (2023) and focusing on the troposphere. Fig. 7a presents the annual mean TROPOMI $NO_2$ columns retrieved using these different a-~~-~~priori profiles, with inter-comparisons shown in Figs. 7b and 7c. Both CAMS-S5P and DACNO$_2$-S5P profiles lead to substantial increases in the retrieved $NO_2$ columns, by 36.2% and 39.8% on average, respectively. The increase associated with CAMS-S5P is consistent with previous findings (Douros et al., 2023) and is primarily attributable to the improved spatial resolution of the a-priori profile, which ~~enhances the sensitivity of TROPOMI retrievals to $NO_2$~~better represents near-surface $NO_2$ enhancements and fine-scale spatial gradients, resulting in larger retrieved tropospheric columns over emission hotspots (Tack et al., 2021; Ialongo et al., 2020).

Compared to the CAMS-S5P profile, using DACNO$_2$-S5P as the a-~~-~~priori increases retrieved $NO_2$ columns by about 3.0% on average (Fig. 7b), associated with the reduced negative bias against EEA-S5P measurements reported above. This change is accompanied by a clear spatial structure in the differences, with localized increases over small-scale emission hotspots and decreases over low-emission regions. In central-western France (0°E–2.6°E, 45.6°N–46.3°N), a distinct southwest-to-northeast line of reinforced $NO_2$ columns appears because DACNO$_2$-S5P enhances the emission signals from the cities of Angoulême, Guéret, and Montluçon. Regional comparisons (Fig. 7c) show that the DACNO$_2$-S5P profile leads to a 1.8% increase in the northern region and 5.9% in Paris, with the most significant increases surrounding major emission hotspots. This is likely due to DACNO$_2$'s enhanced ability, based on finer resolution, to capture small-scale emission sources and resolve strong spatial gradients around $NO_2$ hotspots. In the Alpine region, the average increase reaches 1.7%, ranging from -18.1% (5th percentile) to +24.1% (95th percentile) between the surrounding areas and the central mountains, with a similar pattern observed in the Pyrenees. The absolute difference remains small, ranging from $-3.94 \times 10^{14}$ molecules/cm$^2$ (5th percentile) to $5.39 \times 10^{14}$ molecules/cm$^2$ (95th percentile). This large fluctuation reflects the complex $NO_2$ distribution in the mountainous region and benefits from high-resolution modeling, as DACNO$_2$ estimates can reach lower background values or enhance the hotspots signal in this region.

These results illustrate the potential of using DACNO$_2$ profiles to improve satellite NO$_2$ retrievals, particularly for evolving high-resolution instruments. However, the DACNO$_2$ product remains a prototype, and ~~a~~we outline a brief roadmap for operational deployment ~~is outlined~~ in the conclusion section. In addition, DACNO$_2$ provides a-priori NO$_2$ profiles up to 5000 m, while NO$_2$ signals at roughly 8 – 12 km show a slight enhancement, possibly linked to aviation and lightning (Douros et al., 2023; Kuhn et al., 2024a; Dahlmann et al., 2011; Richter, 2009). This should also be considered in future DACNO$_2$ development.

### 4.4 Generalization Capability and Data Quality: Insights from the COVID-19 Period

**Table 3. Performance of DACNO$_2$ on the 2020 dataset.**

| Year 2020 (2 km × 2 km) | DACNO$_2$-Phase-2 | | | | DACNO$_2$-Phase-3-2020 | | | | CAMS-2020-2km | | | |
|---|---|---|---|---|---|---|---|---|---|---|---|---|
| EEA | RMSE (ug/m$^3$) | r | $R^2$ | bias (ug/m$^3$) | RMSE (ug/m$^3$) | r | $R^2$ | bias (ug/m$^3$) | RMSE (ug/m$^3$) | r | $R^2$ | bias (ug/m$^3$) |
| Total | 5.78 | 0.80 | 0.63 | -0.27 | 5.47 | 0.82 | 0.67 | **0.01*** | **4.99*** | **0.88*** | **0.73*** | -2.05 |
| Urban | 6.06 | 0.81 | 0.63 | -1.53 | **5.62*** | 0.83 | **0.68*** | **-1.28*** | 5.83 | **0.88*** | 0.65 | -3.44 |
| Suburban | 5.81 | 0.80 | 0.58 | 1.12 | 5.63 | 0.82 | 0.60 | 1.55 | **3.97*** | **0.91*** | **0.80*** | **-1.08*** |
| Rural | 4.97 | 0.81 | 0.63 | 1.08 | 4.84 | 0.82 | 0.65 | 1.24 | **3.80*** | **0.89*** | **0.78*** | **0.14*** |

| (10 km × 10 km) | DACNO$_2$-~~10km~~Phase-2 | | | | DACNO$_2$-Phase-3-2020 | | | | |
|---|---|---|---|---|---|---|---|---|---|
| CAMS-2020 | RMSE (ug/m$^3$) | r | $R^2$ | bias (ug/m$^3$) | RMSE (ug/m$^3$) | r | $R^2$ | bias (ug/m$^3$) | |
| ~~Total levels~~All layers | 1.66 | **0.91*** | 0.80 | -0.43 | **1.62*** | **0.91*** | **0.81*** | **-0.34*** | ~~CAMS-2020 (10 km)~~ |
| L0 | 2.18 | 0.93 | 0.84 | **0.43*** | **2.09*** | **0.94*** | **0.86*** | 0.48 | |
| L50 | **1.95*** | 0.93 | **0.84*** | **0.57*** | 2.06 | **0.94*** | 0.82 | 0.77 | |

Inserted Cells

Deleted Cells

| | | | | | | | | |
|---|---|---|---|---|---|---|---|---|
| L250 | 1.97 | **0.89*** | 0.74 | -0.70 | **1.89*** | 0.88 | **0.76*** | **-0.50*** |
| L500 | 2.06 | **0.83*** | 0.50 | -1.01 | **1.94*** | 0.82 | **0.55*** | **-0.81*** |
| L1000 | 1.64 | **0.72*** | 0.00 | -1.01 | **1.57*** | 0.70 | **0.09*** | **-0.93*** |
| L2000 | 1.42 | **0.49*** | -0.81 | -1.01 | **1.40*** | 0.47 | **-0.77*** | **-0.99*** |
| L3000 | 0.81 | **0.46*** | -0.99 | **-0.59*** | **0.80*** | 0.45 | **-0.95*** | **-0.59*** |
| L5000 | **0.17*** | 0.55 | -0.70 | **-0.12*** | **0.17*** | **0.56*** | **-0.64*** | **-0.12*** |

*Note: Similar to Table 2, but for the year 2020.*

As noted in Section 2.4.1, CAMS $NO_2$ data for 2020 were excluded from the training set based on preliminary experiments showing that their inclusion substantially reduced model generalization at higher ~~levels~~layers. Since 2020 was marked by the COVID-19 pandemic and large reductions in anthropogenic emissions (Levelt et al., 2022), we specifically evaluated DACNO$_2$'s predictive performance for this ~~atypical~~anomalous year. To this end, the DACNO$_2$-Phase-2 model was fine-tuned on 2020 EEA $NO_2$ data, following the same phased development strategy, to produce DACNO$_2$-Phase-3-2020.

Table 3 summarizes the 2020 evaluation results, following the format of Table 2. Both DACNO$_2$-Phase-2 and DACNO$_2$-Phase-3-2020 reproduced observed surface $NO_2$ concentrations well (e.g., DACNO$_2$-Phase-3-2020: RMSE = 5.47 μg/m$^3$, r = 0.82, $R^2$ = 0.67, bias = 0.01 μg/m$^3$), with performance comparable to CAMS (RMSE = 4.99 μg/m$^3$, r = 0.88, $R^2$ = 0.73, bias = -2.05 μg/m$^3$) but notably lower bias. ~~This demonstrates robust generalization by DACNO$_2$ under the emission anomalies of the pandemic year.~~ Fig. S5 shows the temporal trend between model estimations and EEA measurements. It is observed that DACNO$_2$-Phase-2 can still capture the temporal trend of $NO_2$ in this unknown and anomalous year, while a positive bias appears during March and May when COVID-19 control measures took place. DACNO$_2$-Phase-3-2020 has successfully reduced the remaining bias with the adaptive fine-tuning. This demonstrates the robustness of the DACNO$_2$ model and the necessity of adaptive fine-tuning to capture anomalous events. Additionally, CAMS maintains overall consistency across measurements but exhibits a pronounced negative bias, primarily in urban areas.

Agreement between DACNO$_2$ and CAMS remains strong at low altitudes (e.g., surface: RMSE = 2.09 μg/m$^3$, r = 0.94, $R^2$ = 0.86, bias = 0.48 μg/m$^3$), but declines rapidly above 1000 m, where $R^2$ values approach zero or become negative, indicating a failure to reproduce high altitude CAMS $NO_2$ distributions for 2020.

~~A comparison~~Comparison of CAMS $NO_2$ vertical distributions from 2019 to 2023 (Fig. ~~S1~~S2) shows generally consistent annual patterns, except for 2020, which is characterized by anomalously high values above 1000 m. This anomaly is also noted in the CAMS 2020 annual evaluation report (Meleux et al., 2023), which attributes it to some sub-models producing unexpectedly high $NO_2$ ~~at high levels~~in the upper layers, resulting in inflated tropospheric column estimates. The underlying causes remain unresolved and require further investigation. These findings highlight the importance of data screening, such as checking distributions and identifying outliers, before model training. Including biased or anomalous target data can introduce noise, increase the risk of overfitting, and reduce generalization performance.

## 5. Conclusions and ~~outlook~~Outlook

This study presents the Deep Atmospheric Chemistry $NO_2$ model ($DACNO_2$), a deep learning model for daily, high-resolution (2 km × 2 km) 3D $NO_2$ estimation. $DACNO_2$ integrates multi-source and multi-modal input features, including emissions, geography, meteorology, and temporal indicators. It uses a multi-constraint and phased training approach to learn from both process-based CAMS $NO_2$ and measured EEA $NO_2$ data. This approach allows $DACNO_2$ to reproduce broad-scale, process-based $NO_2$ patterns and capture local $NO_2$ gradients. Results show that $DACNO_2$ significantly improves the ability to resolve fine-scale spatial patterns, near-surface $NO_2$ variability, and vertical distribution. It also generalizes well across different spatial areas (urban, rural, mountainous, and emission hotspot regions) and periods of anomalous emissions. At the 2 km grid resolution, most spatial detail is provided by high-resolution, time-independent geographic data and emission-related proxies. Meanwhile, large-scale variability is driven primarily by meteorological variables and temporal indicators at coarse scales. The $DACNO_2$ model learns, through a phased training strategy, how these dynamic coarse-scale drivers interact with fine-scale spatial inputs to improve the spatiotemporal representation of the $NO_2$ variability. Furthermore, the framework demonstrates transferability and flexibility, allowing the model to be fine-tuned to adapt to future emission scenarios and to be adjusted to produce outputs for specific satellite overpass times in addition to daily averages.

A systematic evaluation shows that $DACNO_2$ outperforms the state-of-the-art regional CAMS product in reproducing measured surface $NO_2$ concentrations. Overall, $DACNO_2$ achieves a lower RMSE (4.99 vs. 5.32 $\mu g/m^3$), higher correlation ($r = 0.82$ vs. 0.80, $R^2 = 0.66$ vs. 0.61), and a substantially reduced bias (-0.38 vs. -1.15 $\mu g/m^3$). The improvement is ~~particularly significant in~~most evident at urban ~~areas with high~~ sites, where spatial variability~~, where $DACNO_2$ yields a higher $R^2$ (0.64 vs. 0.56)~~ is strongest, and ~~halves~~$DACNO_2$ also reduces the ~~negative~~positive bias ~~(-1.42 vs. -2.89 $\mu g/m^3$). In~~at rural ~~areas~~sites with ~~very~~ low background ~~levels, $DACNO_2$ also shows a better $R^2$ (0.55 vs. 0.51) and maintains a small positive bias, in contrast to the large one from CAMS (1.05 vs. 1.98 $\mu g/m^3$).~~concentrations. Vertical profile analysis indicates that $DACNO_2$ provides greater spatial detail and variation than CAMS, capturing small-scale emission sources and topographic influences more effectively. Feature importance analysis ~~highlights the contribution of~~indicates that high-resolution emission proxies, land cover, and multi-level meteorological ~~information~~variables are key contributors to ~~resolving~~constructing spatial and vertical $NO_2$ patterns. In contrast, single-level meteorological variables ~~contribute minimally~~provide only limited incremental information, likely ~~because part of their information is already captured by the more comprehensive~~ due to some redundancy with the multi-level data~~. This redundancy~~

~~suggests~~, suggesting opportunities for future model optimization. In addition, the EEA-based examination indicates that future EEA constraint usage should consider sample rebalancing and provide sufficient spatial context.

Application to satellite $NO_2$ retrievals demonstrates that using DACNO$_2$-generated a-priori profiles ~~enhances~~makes the ~~sensitivity of~~ TROPOMI $NO_2$ products ~~to~~better account for near-surface concentrations and emission hotspots, particularly ~~in~~for small-scale emission sources and complex geographic regions. These findings underscore the potential of high-resolution ML-based profiles for future high-resolution satellite retrievals. However, DACNO$_2$ remains a prototype, and further work is needed for operational deployment. First, this would involve extending the model's output to continuous hourly profiles ~~over~~across a broader geographic domain and considering profiles above 5000 m. Second, the model would need to be operated on a robust GPU computational platform with automated data pipelines. Third, a routine validation framework would need to be established to continuously monitor performance against various data, such as CAMS $NO_2$, EEA $NO_2$, and vertical measurements (e.g., MAX-DOAS). Finally, this operational system would require a strategy for periodic model fine-tuning to adapt to evolving emission patterns and maintain long-term accuracy.

Analysis of model performance during COVID-19 indicates that DACNO$_2$ consistently generalizes well despite emission anomalies. The inconsistencies observed in CAMS reanalysis for 2020 at high ~~levels~~layers highlight the need for screening and quality assurance in model training data to avoid learning biased patterns and degrading model reliability.

The constraint strategy still needs improvement, as the model's fine-tuning currently relies heavily on surface EEA measurements, which are biased due to uneven distribution, measurement methods, and spatial representativeness. Future development of DACNO$_2$ ~~may include~~ could incorporate constraints above the surface, such as integrating high-resolution 3D process-based $NO_2$ fields from models ~~such as~~(e.g., WRF-Chem) and column observations from satellites ~~to strengthen constraints at higher altitudes (e.g., above~~ , and embedding additional physical constraints into the loss function. Moreover, one can explore~~2000 m), exploring~~ transformer architectures for improved scalability and ~~multi-modal~~multimodal data processing, and ~~embedding additional physical constraints into the loss function. Extension~~extend the model to continental or global applications (including data-poor regions such as the African continent~~)~~). This will further support large-scale air quality management and atmospheric chemistry research.

## Data and code availability

The daily number of flights is accessible at https://www.eurocontrol.int/Economics/DailyTrafficVariation-States.html. The CAMS global emission inventories are accessible at https://ads.atmosphere.copernicus.eu/. The GRIP global roads database can be downloaded from https://www.globio.info/download-grip-dataset. The VIIRS nighttime light data can be accessed from https://eogdata.mines.edu/products/vnl/. The population dataset is provided by https://ec.europa.eu/eurostat/web/gisco/geodata/population-distribution/population-grids. The MERIT DEM data is accessible via https://hydro.iis.u-tokyo.ac.jp/~yamadai/MERIT_DEM/. The CORINE land cover dataset can be downloaded from https://land.copernicus.eu/en/products/corine-land-cover/clc2018. The single-level and multi-level meteorological data are provided by the fifth-generation ECMWF atmospheric reanalysis of the global climate product (ERA5), which can be accessed via https://cds.climate.copernicus.eu/. The CAMS European air quality reanalyses dataset is accessible via https://ads.atmosphere.copernicus.eu/. The EEA AirBase dataset can be downloaded from https://eeadmz1-downloads-webapp.azurewebsites.net/. The official TROPOMI $NO_2$ product is accessible via the Copernicus Data Space Ecosystem (https://dataspace.copernicus.eu/). The data generated for this study can be accessed from the Zenodo data archive (Sun et al. (2025), https://doi.org/10.5281/zenodo.16986854).

The DACNO$_2$ model and its framework are built using the Pytorch library (https://pytorch.org/) in the Python environment. All code related to model design and data processing is available upon request from the corresponding author.

## Author contribution

WS, FT, and MVR conceived the study. WS built the model, performed all analyses, and wrote the initial draft of the manuscript. FT, LC, and MVR reviewed and revised the draft. All authors substantially contributed to the final manuscript.

## Competing interests

The co-author, MVR, is a member of the editorial board of Atmospheric Chemistry and Physics. The other authors declare no competing interests.

**Acknowledgements**

The Belgian Federal Science Policy Office is gratefully appreciated for funding part of this work in the framework of the Terrascope-S5P PRODEX project (PEA 4000136290) and the CAELOSCOPE project (CB/35/16); L.C. is a research associate supported by the Belgian F.R.S.-FNRS. We used AI-assisted tools to polish the manuscript. The authors are solely responsible for the scientific content and interpretations.

**References**


Beelen, R., Hoek, G., Vienneau, D., Eeftens, M., Dimakopoulou, K., Pedeli, X., Tsai, M.-Y., Künzli, N., Schikowski, T., Marcon, A., Eriksen, K. T., Raaschou-Nielsen, O., Stephanou, E., Patelarou, E., Lanki, T., Yli-Tuomi, T., Declercq, C., Falq, G., Stempfelet, M., Birk, M., Cyrys, J., von Klot, S., Nádor, G., Varró, M. J., Dėdelė, A., Gražulevičienė, R., Mölter, A., Lindley, S., Madsen, C., Cesaroni, G., Ranzi, A., Badaloni, C., Hoffmann, B., Nonnemacher, M., Krämer, U., Kuhlbusch, T., Cirach, M., de Nazelle, A., Nieuwenhuijsen, M., Bellander, T., Korek, M., Olsson, D., Strömgren, M., Dons, E., Jerrett, M., Fischer, P., Wang, M., Brunekreef, B., and de Hoogh, K.: Development of $NO_2$ and $NO_x$ land use regression models for estimating air pollution exposure in 36 study areas in Europe – The ESCAPE project, Atmospheric Environment, 72, 10-23, 10.1016/j.atmosenv.2013.02.037, 2013.

Bernd, S., Valerie, F., Bézy, J. L., Meijer, Y., Durand, Y., Courrèges-Lacoste, G. B., Pachot, C., Löscher, A., Nett, H., Minoglou, K., Boucher, L., Windpassinger, R., Pasquet, A., Serre, D., and Hennepe, F. t.: The Copernicus CO2M mission for monitoring anthropogenic carbon dioxide emissions from space, Proc.SPIE, 118523M, 10.1117/12.2599613,

Bey, I., Jacob, D. J., Yantosca, R. M., Logan, J. A., Field, B. D., Fiore, A. M., Li, Q. B., Liu, H. G. Y., Mickley, L. J., and Schultz, M. G.: Global modeling of tropospheric chemistry with assimilated meteorology: Model description and evaluation, Journal of Geophysical Research-Atmospheres, 106, 23073–23095, 10.1029/2001jd000807, 2001.

Bézy, J.-L., Sierk, B., Caron, J., Veihelmann, B., Martin, D., and Langen, J.: The Copernicus Sentinel-5 mission for operational atmospheric monitoring: status and developments, SPIE Remote Sensing, SPIE, 10.1117/12.2068177, 2014.

Bi, K., Xie, L., Zhang, H., Chen, X., Gu, X., and Tian, Q.: Accurate medium-range global weather forecasting with 3D neural networks, Nature, 619, 533-538, 10.1038/s41586-023-06185-3, 2023.

Bodnar, C., Bruinsma, W. P., Lucic, A., Stanley, M., Allen, A., Brandstetter, J., Garvan, P., Riechert, M., Weyn, J. A., Dong, H., Gupta, J. K., Thambiratnam, K., Archibald, A. T., Wu, C.-C., Heider, E., Welling, M., Turner, R. E., and Perdikaris, P.: A foundation model for the Earth system, Nature, 641, 1180-1187, 10.1038/s41586-025-09005-y, 2025.

Bodnar, C., Bruinsma, W. P., Lucic, A., Stanley, M., Vaughan, A., Brandstetter, J., Garvan, P., Riechert, M., Weyn, J. A., Dong, H., Gupta, J. K., Thambiratnam, K., Archibald, A. T., Wu, C.-C., Heider, E., Welling, M., Turner, R. E., and Perdikaris, P.: A Foundation Model for the Earth System, 10.48550/arXiv.2405.13063, 2024.

Castellanos, P. and Boersma, K. F.: Reductions in nitrogen oxides over Europe driven by environmental policy and economic recession, Scientific Reports, 2, 265, 10.1038/srep00265, 2012.

Chang, S. Y., Huang, J., Chaveste, M. R., Lurmann, F. W., Eisinger, D. S., Mukherjee, A. D., Erdakos, G. B., Alexander, M., and Knipping, E.: Electric vehicle fleet penetration helps address inequalities in air quality and improves environmental justice, Communications Earth & Environment, 4, 135, 10.1038/s43247-023-00799-1, 2023.

CAMS Regional: European air quality reanalyses data documentation: https://confluence.ecmwf.int/display/CKB/CAMS+Regional%3A+European+air+quality+reanalyses+data+documentation, last access: June 2024.

Crippa, M., Guizzardi, D., Muntean, M., Schaaf, E., Dentener, F., van Aardenne, J. A., Monni, S., Doering, U., Olivier, J. G. J., Pagliari, V., and Janssens-Maenhout, G.: Gridded emissions of air pollutants for the period 1970–2012 within EDGAR v4.3.2, Earth System Science Data, 10, 1987-2013, 10.5194/essd-10-1987-2018, 2018.

Dahlmann, K., Grewe, V., Ponater, M., and Matthes, S.: Quantifying the contributions of individual $NO_x$ sources to the trend in ozone radiative forcing, Atmospheric Environment, 45, 2860-2868, 10.1016/j.atmosenv.2011.02.071, 2011.

Dijkstra, L., Florczyk, A. J., Freire, S., Kemper, T., Melchiorri, M., Pesaresi, M., and Schiavina, M.: Applying the Degree of Urbanisation to the globe: A new harmonised definition reveals a different picture of global urbanisation, Journal of Urban Economics, 125, 103312, 10.1016/j.jue.2020.103312, 2021.

Ding, N., Qin, Y., Yang, G., Wei, F., Yang, Z., Su, Y., Hu, S., Chen, Y., Chan, C.-M., Chen, W., Yi, J., Zhao, W., Wang, X., Liu, Z., Zheng, H.-T., Chen, J., Liu, Y., Tang, J., Li, J., and Sun, M.: Parameter-efficient fine-tuning of large-scale pre-trained language models, Nature Machine Intelligence, 5, 220-235, 10.1038/s42256-023-00626-4, 2023.

Douros, J., Eskes, H., van Geffen, J., Boersma, K. F., Compernolle, S., Pinardi, G., Blechschmidt, A. M., Peuch, V. H., Colette, A., and Veefkind, P.: Comparing Sentinel-5P TROPOMI $NO_2$ column observations with the CAMS regional air quality ensemble, Geoscientific Model Development, 16, 509-534, 10.5194/gmd-16-509-2023, 2023.

Elfwing, S., Uchibe, E., and Doya, K.: Sigmoid-Weighted Linear Units for Neural Network Function Approximation in Reinforcement Learning, 10.48550/arXiv.1702.03118, 2017.

Elvidge, C. D., Zhizhin, M., Ghosh, T., Hsu, F.-C., and Taneja, J.: Annual Time Series of Global VIIRS Nighttime Lights Derived from Monthly Averages: 2012 to 2019, Remote Sensing, 13, 10.3390/rs13050922, 2021.

Eurocontrol: Daily traffic variation for states [dataset], https://www.eurocontrol.int/Economics/2020-DailyTrafficVariation-States.html, 2025.

AirBase - The European air quality database: https://eeadmz1-downloads-webapp.azurewebsites.net/, last access: June 2024.

Feranec, J., Soukup, T., Hazeu, G., and Jaffrain, G.: European Landscape Dynamics CORINE Land Cover Data, in, CRC Press, Boca Raton, 367, 10.1201/9781315372860, 2016.

Ghahremanloo, M., Lops, Y., Choi, Y., Mousavinezhad, S., and Jung, J.: A Coupled Deep Learning Model for Estimating Surface $NO_2$ Levels From Remote Sensing Data: 15-Year Study Over the Contiguous United States, Journal of Geophysical Research: Atmospheres, 128, e2022JD037010, 10.1029/2022JD037010, 2023.

Giovannini, L., Ferrero, E., Karl, T., Rotach, M. W., Staquet, C., Trini Castelli, S., and Zardi, D.: Atmospheric Pollutant Dispersion over Complex Terrain: Challenges and Needs for Improving Air Quality Measurements and Modeling, Atmosphere, 11, 646, 10.3390/atmos11060646, 2020.

Grell, G. A., Peckham, S. E., Schmitz, R., McKeen, S. A., Frost, G., Skamarock, W. C., and Eder, B.: Fully coupled "online" chemistry within the WRF model, Atmospheric Environment, 39, 6957-6975, 10.1016/j.atmosenv.2005.04.027, 2005.

Gulde, S., Kolm, M., Smith, D., Maurer, R., Courrèges-Lacoste, G. B., Sallusti, M., and Bagnasco, G.: Sentinel 4: a geostationary imaging UVN spectrometer for air quality monitoring: status of design, performance and development, International Conference on Space Optics—ICSO 2014, Tenerife, Canary Islands, Spain, 1158-1166, 10.1117/12.2304099,

He, K., Zhang, X., Ren, S., and Sun, J.: Deep Residual Learning for Image Recognition, 2016 IEEE Conference on Computer Vision and Pattern Recognition (CVPR), Las Vegas, NV, USA, 27-30 June 2016, 1, 10.1109/cvpr.2016.90,

Hersbach, H., Bell, B., Berrisford, P., Hirahara, S., Horányi, A., Muñoz-Sabater, J., Nicolas, J., Peubey, C., Radu, R., Schepers, D., Simmons, A., Soci, C., Abdalla, S., Abellan, X., Balsamo, G., Bechtold, P., Biavati, G., Bidlot, J., Bonavita, M., De Chiara, G., Dahlgren, P., Dee, D., Diamantakis, M., Dragani, R., Flemming, J., Forbes, R., Fuentes, M., Geer, A., Haimberger, L., Healy, S., Hogan, R. J., Hólm, E., Janisková, M., Keeley, S., Laloyaux, P., Lopez, P., Lupu, C., Radnoti, G., de Rosnay, P., Rozum, I., Vamborg, F., Villaume, S., and Thépaut, J.-N.: The ERA5 global reanalysis, Quarterly Journal of the Royal Meteorological Society, 146, 1999-2049, 10.1002/qj.3803, 2020.

Hochreiter, S. and Schmidhuber, J.: Long Short-Term Memory, Neural Computation, 9, 1735-1780, 10.1162/neco.1997.9.8.1735, 1997.

Huijnen, V., Williams, J., van Weele, M., van Noije, T., Krol, M., Dentener, F., Segers, A., Houweling, S., Peters, W., de Laat, J., Boersma, F., Bergamaschi, P., van Velthoven, P., Le Sager, P., Eskes, H., Alkemade, F., Scheele, R., Nédélec, P., and Pätz, H. W.: The global chemistry transport model TM5: description and evaluation of the tropospheric chemistry version 3.0, ~~Geosci.~~Geoscientific Model ~~Dev.,~~Development, 3, 445-473, 10.5194/gmd-3-445-2010, 2010.

Ialongo, I., Virta, H., Eskes, H., Hovila, J., and Douros, J.: Comparison of TROPOMI/Sentinel-5 Precursor $NO_2$ observations with ground-based measurements in Helsinki, ~~Atmos. Meas. Tech.,~~Atmospheric Measurement Techniques, 13, 205-218, 10.5194/amt-13-205-2020, 2020.

Inness, A., Ades, M., Agustí-Panareda, A., Barré, J., Benedictow, A., Blechschmidt, A. M., Dominguez, J. J., Engelen, R., Eskes, H., Flemming, J., Huijnen, V., Jones, L., Kipling, Z., Massart, S., Parrington, M., Peuch, V. H., Razinger, M., Remy, S., Schulz, M., and Suttie, M.: The CAMS reanalysis of atmospheric composition, Atmospheric Chemistry and Physics, 19, 3515-3556, 10.5194/acp-19-3515-2019, 2019.

Ioffe, S. and Szegedy, C.: Batch Normalization: Accelerating Deep Network Training by Reducing Internal Covariate Shift, Proceedings of the 32nd International Conference on Machine Learning, Proceedings of Machine Learning Research, 10.5555/3045118.3045167, 2015.

Jiang, Z., Wang, S., Yan, Y., Zhang, S., Xue, R., Gu, C., Zhu, J., Liu, J., and Zhou, B.: Constructing the 3D Spatial Distribution of the $HCHO/NO_2$ Ratio via Satellite Observation and Machine Learning Model, Environmental Science & Technology, 59, 4047-4058, 10.1021/acs.est.4c12362, 2025.

Kim, J., Jeong, U., Ahn, M.-H., Kim, J. H., Park, R. J., Lee, H., Song, C. H., Choi, Y.-S., Lee, K.-H., Yoo, J.-M., Jeong, M.-J., Park, S. K., Lee, K.-M., Song, C.-K., Kim, S.-W., Kim, Y. J., Kim, S.-W., Kim, M., Go, S., Liu, X., Chance, K., Chan Miller, C., Al-Saadi, J., Veihelmann, B., Bhartia, P. K., Torres, O., Abad, G. G., Haffner, D. P., Ko, D. H., Lee, S. H., Woo, J.-H., Chong, H., Park, S. S., Nicks, D., Choi, W. J., Moon, K.-J., Cho, A., Yoon, J., Kim, S.-k., Hong, H., Lee, K., Lee, H., Lee, S., Choi, M., Veefkind, P., Levelt, P. F., Edwards, D. P., Kang, M., Eo, M., Bak, J., Baek, K., Kwon, H.-A., Yang, J., Park, J., Han, K. M., Kim, B.-R., Shin, H.-W., Choi, H., Lee, E., Chong, J., Cha, Y., Koo, J.-H., Irie, H., Hayashida, S., Kasai,

Y., Kanaya, Y., Liu, C., Lin, J., Crawford, J. H., Carmichael, G. R., Newchurch, M. J., Lefer, B. L., Herman, J. R., Swap, R. J., Lau, A. K. H., Kurosu, T. P., Jaross, G., Ahlers, B., Dobber, M., McElroy, C. T., and Choi, Y.: New era of air quality monitoring from space: Geostationary Environment Monitoring Spectrometer (GEMS), Bulletin of the American Meteorological Society, 101, E1-E22, 10.1175/bams-d-18-0013.1, 2020.

Kim, M., Brunner, D., and Kuhlmann, G.: Importance of satellite observations for high-resolution mapping of near-surface $NO_2$ by machine learning, Remote Sensing of Environment, 264, 112573, 10.1016/j.rse.2021.112573, 2021.

Kokhlikyan, N., Miglani, V., Martin, M., Wang, E., Alsallakh, B., Reynolds, J., Melnikov, A., Kliushkina, N., Araya, C., Yan, S., and Reblitz-Richardson, O.: Captum: A unified and generic model interpretability library for PyTorch, arXiv:2009.07896, 10.48550/arXiv.2009.07896, 2020.

Kracht, O., Santiago, J. L., Martin, F., Piersanti, A., Cremona, G., Righini, G., Vitali, L., Delaney, K., Basu, B., Ghosh, B., Spangl, W., Brendle, C., Latikka, J., Kousa, A., Pärjälä, E., Meretoja, M., Malherbe, L., Letinois, L., Beauchamp, M., Lenartz, F., Hutsemekers, V., Nguyen, L., Hoogerbrugge, R., Eneroth, K., Silvergren, S., Hooyberghs, H., Viaene, P., Maiheu, B., Janssen, S., Roet, D., and Gerboles, M.: Spatial representativeness of air quality monitoring sites – Outcomes of the FAIRMODE/AQUILA intercomparison exercise, Publications Office of the European Union, 10.2760/60611, 2017.

Krol, M., Houweling, S., Bregman, B., van den Broek, M., Segers, A., van Velthoven, P., Peters, W., Dentener, F., and Bergamaschi, P.: The two-way nested global chemistry-transport zoom model TM5: algorithm and applications, ~~Atmos. Chem. Phys.,~~Atmospheric Chemistry and Physics, 5, 417-432, 10.5194/acp-5-417-2005, 2005.

Kuhn, L., Beirle, S., Osipov, S., Pozzer, A., and Wagner, T.: NitroNet – a machine learning model for the prediction of tropospheric $NO_2$ profiles from TROPOMI observations, ~~Atmos. Meas. Tech.,~~Atmospheric Measurement Techniques, 17, 6485-6516, 10.5194/amt-17-6485-2024, 2024a.

Kuhn, L., Beirle, S., Kumar, V., Osipov, S., Pozzer, A., Bösch, T., Kumar, R., and Wagner, T.: On the influence of vertical mixing, boundary layer schemes, and temporal emission profiles on tropospheric $NO_2$ in WRF-Chem – comparisons to in situ, satellite, and MAX-DOAS observations, ~~Atmos. Chem. Phys.,~~Atmospheric Measurement Techniques, 24, 185-217, 10.5194/acp-24-185-2024, 2024b.

Kuik, F., Kerschbaumer, A., Lauer, A., Lupascu, A., von Schneidemesser, E., and Butler, T. M.: Top–down quantification of $NO_x$ emissions from traffic in an urban area using a high-resolution regional atmospheric chemistry model, ~~Atmos. Chem. Phys.,~~Atmospheric Chemistry and Physics, 18, 8203-8225, 10.5194/acp-18-8203-2018, 2018.

Lam, R., Sanchez-Gonzalez, A., Willson, M., Wirnsberger, P., Fortunato, M., Alet, F., Ravuri, S., Ewalds, T., Eaton-Rosen, Z., Hu, W., Merose, A., Hoyer, S., Holland, G., Vinyals, O., Stott, J., Pritzel, A., Mohamed, S., and Battaglia, P.: Learning skillful medium-range global weather forecasting, Science, 382, 1416-1421, doi:10.1126/science.adi2336, 2023.

Lamsal, L. N., Martin, R. V., van Donkelaar, A., Steinbacher, M., Celarier, E. A., Bucsela, E., Dunlea, E. J., and Pinto, J. P.: Ground-level nitrogen dioxide concentrations inferred from the satellite-borne Ozone Monitoring Instrument, Journal of Geophysical Research: Atmospheres, 113, 10.1029/2007JD009235, 2008.

Landgraf, J., Rusli, S., Cooney, R., Veefkind, P., Vemmix, T., de Groot, Z., Bell, A., Day, J., Leemhuis, A., and Sierk, B.: The TANGO mission: A satellite tandem to measure major sources of anthropogenic greenhouse gas emissions, EGU General Assembly Conference Abstracts, 19643,

Levelt, P. F., Stein Zweers, D. C., Aben, I., Bauwens, M., Borsdorff, T., De Smedt, I., Eskes, H. J., Lerot, C., Loyola, D. G., Romahn, F., Stavrakou, T., Theys, N., Van Roozendael, M., Veefkind, J. P., and Verhoelst, T.: Air quality impacts of COVID-19 lockdown measures detected from space using high spatial resolution observations of multiple trace gases from Sentinel-5P/TROPOMI, Atmospheric Chemistry and Physics, 22, 10319-10351, 10.5194/acp-22-10319-2022, 2022.

Li, S. and Xing, J.: DeepSAT4D: Deep learning empowers four-dimensional atmospheric chemical concentration and emission retrieval from satellite, The Innovation Geoscience, 2, 100061, 10.59717/j.xinn-geo.2024.100061, 2024.

Lu, L., Cohen, J. B., Qin, K., Li, X., and He, Q.: Identifying missing sources and reducing $NO_x$ emissions uncertainty over China using daily satellite data and a mass-conserving method, ~~Atmos. Chem. Phys.,~~Atmospheric Chemistry and Physics, 25, 2291-2309, 10.5194/acp-25-2291-2025, 2025.

Meijer, J. R., Huijbregts, M. A. J., Schotten, K. C. G. J., and Schipper, A. M.: Global patterns of current and future road infrastructure, Environmental Research Letters, 13, 064006, 10.1088/1748-9326/aabd42, 2018.

Meleux, F., Raux, B., Ung, A., Colette, A., Gauss, M., Douros, J., Tsikerdekis, T., and Bennouna, Y.: Annual report on the evaluation of validated reanalyses VRA2020, https://atmosphere.copernicus.eu/sites/default/files/custom-uploads/EQC-regional/VRA/CAMS283_2021SC1_D83.2.2.1-2020_202303_VRA2020_evaluation_v2.pdf, 2023.

Meleux, F., Raux, B., Ung, A., Colette, A., Gauss, M., Douros, J., Tsikerdekis, T., Eskes, H., Bennouna, Y., and Thouret, V.: Annual EQC report for the interim reanalysis for 2023, for each of the operational systems and the ENSEMBLE, https://atmosphere.copernicus.eu/sites/default/files/custom-uploads/EQC-regional/IRA/CAMS283_2021SC2_D83.2.1.1-2023_202406_EQC_IRA2023_v1.pdf, 2024.

Oppenheim, A. V.: Discrete-time signal processing, Pearson Education India1999.

Palmer, P. I., Jacob, D. J., Chance, K., Martin, R. V., Spurr, R. J. D., Kurosu, T. P., Bey, I., Yantosca, R., Fiore, A., and Li, Q.: Air mass factor formulation for spectroscopic measurements from satellites: Application to formaldehyde retrievals from the Global Ozone Monitoring Experiment, Journal of Geophysical Research: Atmospheres, 106, 14539-14550, 10.1029/2000JD900772, 2001.

Peuch, V.-H., Engelen, R., Rixen, M., Dee, D., Flemming, J., Suttie, M., Ades, M., Agustí-Panareda, A., Ananasso, C., Andersson, E., Armstrong, D., Barré, J., Bousserez, N., Dominguez, J. J., Garrigues, S., Inness, A., Jones, L., Kipling, Z., Letertre-Danczak, J., Parrington, M., Razinger, M., Ribas, R., Vermoote, S., Yang, X., Simmons, A., Garcés de Marcilla, J., and Thépaut, J.-N.: The Copernicus Atmosphere Monitoring Service: From Research to Operations, Bulletin of the American Meteorological Society, 103, E2650-E2668, 10.1175/BAMS-D-21-0314.1, 2022.

Richter, A.: Nitrogen oxides in the troposphere – What have we learned from satellite measurements?, EPJ Web of Conferences, 1, 149-156, 10.1140/epjconf/e2009-00916-9, 2009.

Shahrokhishahraki, N., Rayner, P. J., Silver, J. D., Thomas, S., and Schofield, R.: High-resolution modeling of gaseous air pollutants over Tehran and validation with surface and satellite data, Atmospheric Environment, 270, 118881, 10.1016/j.atmosenv.2021.118881, 2022.

Shi, X., Chen, Z., Wang, H., Yeung, D.-Y., Wong, W.-k., and Woo, W.-c.: Convolutional LSTM Network: A Machine Learning Approach for Precipitation Nowcasting, 10.48550/arXiv.1506.04214, 2015.

Silva, F. B. e., Poelman, H., and Dijkstra, L.: JRC-GEOSTAT 2018 [dataset], 2021.

Soulie, A., Granier, C., Darras, S., Zilbermann, N., Doumbia, T., Guevara, M., Jalkanen, J. P., Keita, S., Liousse, C., Crippa, M., Guizzardi, D., Hoesly, R., and Smith, S. J.: Global anthropogenic emissions (CAMS-GLOB-ANT) for the Copernicus Atmosphere Monitoring Service simulations of air quality forecasts and reanalyses, Earth ~~Syst. Sci.~~System Science Data, 16, 2261-2279, 10.5194/essd-16-2261-2024, 2024.

Srivastava, N., Hinton, G., Krizhevsky, A., Sutskever, I., and Salakhutdinov, R.: Dropout: a simple way to prevent neural networks from overfitting, Journal of Machine Learning Research, 15, 1929–1958, 10.5555/2627435.2670313, 2014.

Sun, W., Tack, F., Clarisse, L., and Roozendael, M. V.: Technical Note: DACNO$_2$ – A Multi-Constraint Deep Learning Framework for High-Resolution 3D NO$_2$ Field Estimation (Version 1) [dataset], 10.5281/zenodo.16986854, 2025.

Sun, W., Tack, F., Clarisse, L., Schneider, R., Stavrakou, T., and Van Roozendael, M.: Inferring Surface NO$_2$ Over Western Europe: A Machine Learning Approach With Uncertainty Quantification, Journal of Geophysical Research: Atmospheres, 129, e2023JD040676, 10.1029/2023JD040676, 2024.

Sundararajan, M., Taly, A., and Yan, Q.: Axiomatic Attribution for Deep Networks, 10.48550/arXiv.1703.01365, 2017.

Szegedy, C., Vanhoucke, V., Ioffe, S., Shlens, J., and Wojna, Z.: Rethinking the Inception Architecture for Computer Vision, arXiv e-prints, arXiv:1512.00567, 10.48550/arXiv.1512.00567, 2015.

Szegedy, C., Liu, W., Jia, Y., Sermanet, P., Reed, S., Anguelov, D., Erhan, D., Vanhoucke, V., and Rabinovich, A.: Going Deeper with Convolutions, arXiv:1409.4842, 10.48550/arXiv.1409.4842,- 2014.

Tack, F., Merlaud, A., Iordache, M. D., Pinardi, G., Dimitropoulou, E., Eskes, H., Bomans, B., Veefkind, P., and Van Roozendael, M.: Assessment of the TROPOMI tropospheric NO$_2$ product based on airborne APEX observations, Atmospheric Measurement Techniques, 14, 615-646, 10.5194/amt-14-615-2021, 2021.

Veefkind, J. P., Aben, I., McMullan, K., Förster, H., de Vries, J., Otter, G., Claas, J., Eskes, H. J., de Haan, J. F., Kleipool, Q., van Weele, M., Hasekamp, O., Hoogeveen, R., Landgraf, J., Snel, R., Tol, P., Ingmann, P., Voors, R., Kruizinga, B., Vink, R., Visser, H., and Levelt, P. F.: TROPOMI on the ESA Sentinel-5 Precursor: A GMES mission for global observations of the atmospheric composition for climate, air quality and ozone layer applications, Remote Sensing of Environment, 120, 70-83, 10.1016/j.rse.2011.09.027, 2012.

Villena, G., Bejan, I., Kurtenbach, R., Wiesen, P., and Kleffmann, J.: Interferences of commercial NO$_2$ instruments in the urban atmosphere and in a smog chamber, Atmospheric Measurement Techniques, 5, 149-159, 10.5194/amt-5-149-2012, 2012.

Wang, L., Chen, X., Zhang, Y., Li, M., Li, P., Jiang, L., Xia, Y., Li, Z., Li, J., Wang, L., Hou, T., Liu, W., Rosenfeld, D., Zhu, T., Zhang, Y., Chen, J., Wang, S., Huang, Y., Seinfeld, J. H., and Yu, S.: Switching to electric vehicles can lead to significant reductions of PM$_{2.5}$ and NO$_2$ across China, One Earth, 4, 1037-1048, 10.1016/j.oneear.2021.06.008, 2021.

Wei, J., Liu, S., Li, Z., Liu, C., Qin, K., Liu, X., Pinker, R. T., Dickerson, R. R., Lin, J., Boersma, K. F., Sun, L., Li, R., Xue, W., Cui, Y., Zhang, C., and Wang, J.: Ground-Level $NO_2$ Surveillance from Space Across China for High Resolution Using Interpretable Spatiotemporally Weighted Artificial Intelligence, Environmental Science & Technology, 56, 9988-9998, 10.1021/acs.est.2c03834, 2022.

Williams, J. E., Boersma, K. F., Le Sager, P., and Verstraeten, W. W.: The high-resolution version of TM5-MP for optimized satellite retrievals: description and validation, ~~Geosci.~~Geoscientific Model ~~Dev.,~~Development, 10, 721-750, 10.5194/gmd-10-721-2017, 2017.

Yamazaki, D., Ikeshima, D., Tawatari, R., Yamaguchi, T., O'Loughlin, F., Neal, J. C., Sampson, C. C., Kanae, S., and Bates, P. D.: A high-accuracy map of global terrain elevations, Geophysical Research Letters, 44, 5844-5853, 10.1002/2017GL072874, 2017.

Yang, L. H., Jacob, D. J., Colombi, N. K., Zhai, S., Bates, K. H., Shah, V., Beaudry, E., Yantosca, R. M., Lin, H., Brewer, J. F., Chong, H., Travis, K. R., Crawford, J. H., Lamsal, L. N., Koo, J. H., and Kim, J.: Tropospheric $NO_2$ vertical profiles over South Korea and their relation to oxidant chemistry: implications for geostationary satellite retrievals and the observation of $NO_2$ diurnal variation from space, ~~Atmos. Chem. Phys.,~~Atmospheric Chemistry and Physics, 23, 2465-2481, 10.5194/acp-23-2465-2023, 2023.

Yang, Y., Zhao, Y., Zhang, L., Zhang, J., Huang, X., Zhao, X., Zhang, Y., Xi, M., and Lu, Y.: Improvement of the satellite-derived $NO_x$ emissions on air quality modeling and its effect on ozone and secondary inorganic aerosol formation in the Yangtze River Delta, China, ~~Atmos. Chem. Phys.,~~Atmospheric Chemistry and Physics, 21, 1191-1209, 10.5194/acp-21-1191-2021, 2021.

Zhang, C., Liu, C., Li, B., Zhao, F., and Zhao, C.: Spatiotemporal neural network for estimating surface $NO_2$ concentrations over north China and their human health impact, Environmental Pollution, 307, 119510, 10.1016/j.envpol.2022.119510, 2022a.

Zhang, S., Li, B., Liu, L., Hu, Q., Liu, H., Zheng, R., Zhu, Y., Liu, T., Sun, M., and Liu, C.: Prediction of Vertical Profile of ~~NO2~~$NO_2$ Using Deep Multimodal Fusion Network Based on the Ground-Based 3-D Remote Sensing, IEEE Transactions on Geoscience and Remote Sensing, 60, 1-13, 10.1109/TGRS.2021.3061476, 2022b.

Zhang, Z., Li, Q., Hu, Q., Xue, J., Liu, T., Tang, Z., Wang, F., Zhang, C., Lu, C., Wang, Z., Gao, M., and Liu, C.: Deep learning approach for reconstructing three-dimensional distribution of $NO_2$ on an urban scale, Remote Sensing of Environment, 321, 114678, 10.1016/j.rse.2025.114678, 2025.

Zhao, H., Gallo, O., Frosio, I., and Kautz, J.: Loss Functions for Image Restoration With Neural Networks, IEEE Transactions on Computational Imaging, 3, 47-57, 10.1109/TCI.2016.2644865, 2017.

Zhou, W., Bovik, A. C., Sheikh, H. R., and Simoncelli, E. P.: Image quality assessment: from error visibility to structural similarity, IEEE Transactions on Image Processing, 13, 600-612, 10.1109/TIP.2003.819861, 2004.

Zhou, Z., Shin, J., Zhang, L., Gurudu, S., Gotway, M., and Liang, J.: Fine-Tuning Convolutional Neural Networks for Biomedical Image Analysis: Actively and Incrementally, 2017 IEEE Conference on Computer Vision and Pattern Recognition (CVPR), 21-26 July 2017, 4761-4772, 10.1109/CVPR.2017.506,

Zhuang, F., Qi, Z., Duan, K., Xi, D., Zhu, Y., Zhu, H., Xiong, H., and He, Q.: A Comprehensive Survey on Transfer Learning, arXiv:1911.02685, 10.48550/arXiv.1911.02685,- 2019.

Zoogman, P., Liu, X., Suleiman, R. M., Pennington, W. F., Flittner, D. E., Al-Saadi, J. A., Hilton, B. B., Nicks, D. K., Newchurch, M. J., Carr, J. L., Janz, S. J., Andraschko, M. R., Arola, A., Baker, B. D., Canova, B. P., Chan Miller, C., Cohen, R. C., Davis, J. E., Dussault, M. E., Edwards, D. P., Fishman, J., Ghulam, A., González Abad, G., Grutter, M., Herman, J. R., Houck, J., Jacob, D. J., Joiner, J., Kerridge, B. J., Kim, J., Krotkov, N. A., Lamsal, L., Li, C., Lindfors, A., Martin, R. V., McElroy, C. T., McLinden, C., Natraj, V., Neil, D. O., Nowlan, C. R., O'Sullivan, E. J., Palmer, P. I., Pierce, R. B., Pippin, M. R., Saiz-Lopez, A., Spurr, R. J. D., Szykman, J. J., Torres, O., Veefkind, J. P., Veihelmann, B., Wang, H., Wang, J., and Chance, K.: Tropospheric emissions: Monitoring of pollution (TEMPO), Journal of Quantitative Spectroscopy and Radiative Transfer, 186, 17-39, 10.1016/j.jqsrt.2016.05.008, 2017.